

# Dwarf Spheroidal Satellite Formation in a Reionized Local Group

Miloš Milosavljević and Volker Bromm

*Department of Astronomy, The University of Texas at Austin, 2515 Speedway, Stop C1400, Austin, TX 78712*

11 November 2021

## ABSTRACT

Dwarf spheroidal satellite galaxies have emerged a powerful probe of small-scale dark matter clustering and of cosmic reionization. They exhibit structural and chemical continuity with dwarf irregular galaxies in the field and with spheroidal galaxies in high-density environments. By combining empirical constraints derived for star formation at low gas column densities and metallicities in the local universe with a model for dark matter and baryonic mass assembly, we provide an analytical description of how the dwarf spheroidals acquired their stellar content. Their progenitors formed stars until the gas content, initially reduced from the cosmic average by the thermal pressure of the reionized intergalactic medium, was finally ram pressure stripped during the progenitors’ accretion on to the host galaxy. Dwarf spheroidal satellites of differing luminosities seem to share very similar most massive progenitor histories that reach thresholds for gas cooling by atomic line emission at epochs at which the Lagrangian volume of the Local Group should have been reionized. We hypothesize that dwarf spheroidals formed the bulk of their stars in partially rotationally supported HI disks in a reionized universe. This model provides an explanation for the “common mass scale” relation and reproduces the empirical luminosity-size and luminosity-metallicity relations. Explosive feedback phenomena, such as outflows driven by the concerted action of supernovae, need not have been significant in the dwarf spheroidals’ formation. We further speculate that the true pre-reionization fossils should exhibit a structure distinct from that of the dwarf spheroidals, e.g., in the form of dense isolated or nuclear star clusters.

## Key words:

dark ages, reionization, first stars — galaxies: dwarf — galaxies: high-redshift — galaxies: star formation

## 1 INTRODUCTION

The faint satellite galaxies around the Milky Way and Andromeda, the dwarf spheroidals, have been recognized as windows into the clustering of dark matter on small spatial scales (e.g., Lin & Faber 1983; Zentner & Bullock 2003; Gilmore et al. 2007; Boylan-Kolchin et al. 2012). They can also be seen as opportunities for learning about the physics of star formation in the regime in which it is the least efficient, at low gas column densities and low metallicities, where the star formation is the most susceptible to environmental influences such as those arising from cosmic reionization. The discovery of the ultra-faint dwarf spheroidal satellites around the Milky Way (e.g., Willman et al. 2005a,b; Belokurov et al. 2006b, 2007; Sakamoto & Hasegawa 2006; Zucker et al. 2006; Irwin et al. 2007; Walsh et al. 2007) has pushed our ability to measure dark matter mass down to  $\sim 10^6 M_\odot$  on spatial scales of only a few tens of parsecs (e.g., Walker et al. 2009), and has provided us with examples of the smallest and oldest stellar systems known to possess their own dark matter halos (e.g., Brown et al. 2012). Here, in an attempt to explain the structural and chemical trends seen in the dwarf spheroidal population, we present an analytical model

combining constraints derived from investigations of star formation in the local universe with an idealized treatment of the objects’ dark and baryonic mass assembly histories in the standard  $\Lambda$  cold dark matter ( $\Lambda$ CDM) cosmology.

While the dwarf spheroidal satellite galaxies are dark matter dominated, they are arguably the most primitive stellar systems in the local universe, in terms of the relatively small number of stellar generations that entered their formation and the ancient origin of at least some of these stars. The ancient origin, which follows from color-magnitude relation analysis, and indirectly, from the abundances of nucleosynthetic tracers, presents an opportunity for learning about how reionization influenced star formation in the Local Group. The epoch and progress of reionization in the Local Group and in the universe overall are poorly constrained, but it is expected that the dark matter halos hosting dwarf spheroidals had shallow enough gravitational potential wells for reionization to have reduced their gaseous baryonic content (e.g., Bullock et al. 2000). What fraction of the dwarf spheroidals’ stars formed before reionization has been the subject of much investigation, often with coarse-grained cosmological collisionless  $N$ -body or hydrodynamic simulations aided by subgrid prescriptions specifying the

rate of star formation and the intensity of the resulting feedback (e.g., Gnedin & Kravtsov 2006; Bovill & Ricotti 2009, 2011a,b; Muñoz et al. 2009; Busha et al. 2010; Li et al. 2010; Font et al. 2011; Ocvirk & Aubert 2011; Lunnan et al. 2012; Rashkov et al. 2012; Simpson et al. 2013). We take a somewhat different approach and attempt to crudely peg the star formation rate in our model to the measured rate in similar star forming environments in the local universe.

Specifically, evidence emerging from structural correlations is suggesting that dwarf spheroidal galaxies are non-star-forming analogs of dwarf irregular galaxies in the field (Weisz et al. 2011; Kormendy & Bender 2012; Kirby et al. 2013, 2014). The dwarf spheroidals are presently largely gas-free, likely because of stripping during the infall into the host halo, that of the Milky Way or Andromeda (e.g., Grebel et al. 2003; Mayer et al. 2006). The irregulars are still forming stars but the spheroidals ceased star formation at some point in the past. We exploit this evolutionary connection and inform our modeling of star formation in the dwarf spheroidal progenitor objects by the characteristics of star formation in low-surface-density and low-metallicity HI-dominated disks in the nearby universe. This allows us to question the necessity of explosive gas expulsion from dwarf spheroidals, which is occasionally invoked to explain the properties of at least some members of the dwarf spheroidal family (e.g., Read et al. 2006; Sawala et al. 2010; Font et al. 2011; Kirby et al. 2011b).

This work is organized as follows. In Section 2, we use dynamical measurements of the dwarf spheroidals’ central mass densities to constrain their dark matter mass assembly histories. With such histories at hand, in Section 3 we utilize numerical calibrations of the impact of reionization to estimate the evolution of the baryonic gas fraction in the dwarf spheroidals’ progenitor objects. In Section 4, we describe star formation in the progenitor objects, arguing that they formed stars relatively quiescently in what were partially rotationally supported atomic gas flows. In Section 5, we present our results which include estimates of the stellar mass-radius and stellar mass-metallicity relations. Comparing these with the observed dwarfs allows us to estimate the masses and the formation redshifts of the dark matter halos hosting the dwarfs. In Section 6, we briefly discuss where the true pre-reionization fossil stellar systems might be found in the Local Group, and in Section 7, we review our main conclusions. We delegate a number of minor clarifications in instances where the prescriptions we employ diverge from those in the literature to the footnotes.

## 2 DARK MATTER AND MASS ASSEMBLY

### 2.1 The Common Mass Scale Halos Hosting Dwarf Spheroidal Satellites

Dynamical estimates of the masses enclosed within 300 pc of the galaxy center in the Local Group dwarf spheroidals with luminosities  $\lesssim 10^7 L_\odot$  seem to be consistent among most of the dwarfs, suggesting a “common mass scale” of

$$M_{300} \approx 10^7 M_\odot \quad (1)$$

within this radius (Strigari et al. 2008, hereafter S08). This mass seems independent of the galaxy luminosity, though there is a significant scatter, especially at low luminosities, where the enclosed mass is measured at radii smaller than 300 pc and the value of  $M_{300}$  is then estimated by extrapolation assuming a density profile of the NFW form (Navarro et al. 1996). Such extrapolation is meaningful

in principle because dark matter strongly dominates the gravitational potential in dwarf spheroidals, especially at low luminosities. In what follows, we refer to the relation  $M_{300} = 10^7 M_\odot$  as *the* common mass scale family, but we also carefully explore the dependence of our results on the variation of  $M_{300}$ . This additional degree of freedom allows us to classify all dark matter halos by their value of  $M_{300}$  and thus discuss alternative common mass scale families that are more or less dense than the one identified in S08.

Measurements of the dwarf spheroidals’ dynamical masses can be used to place a simple constraint on the mass and epoch of their mass assembly histories. The density profile of an isolated halo evolves continuously as the halo accretes matter and merges with other halos. In this fashion, halos grow in radius and mass and their concentrations evolve. The concentrations of low-mass halos corresponding to low- $\sigma$  cosmic peaks increase with time because these halos grow slowly, allowing for a low-density envelope to accrete around a denser core (Wechsler et al. 2002). Since the radius of 300 pc is much smaller than the virial radius of galaxy-hosting halos at the present epoch, the mass contributing to  $M_{300}$  must have collapsed at an early epoch, when the universe was denser.

The mass assembly of a dwarf spheroidal host halo is truncated by the non-linear tidal field at a critical time preceding its eventual infall into a larger halo, that of the Milky Way, Andromeda, or one of their main progenitors. Recent numerical simulations of CDM clustering suggest that the mass assembly of a small dark matter halo is truncated when the halo approaches to within  $\sim 3$  virial radii of the larger host halo (R. Wechsler, priv. comm.). At  $\sim 1.5$  virial radii of the larger halo, tidal stripping starts reducing the mass of the smaller halo (e.g., Hahn et al. 2009, see also Wang et al. 2007; Dalal et al. 2008). The subhalo’s outer layers are stripped but its densest central cusp can remain intact, a frozen-in relic of an earlier epoch, perhaps substantially preceding the infall.

The development that follows applies to dwarf spheroidal satellites with such preserved central cusps. Our operating assumption is that the tidal stripping has not removed significant stellar mass from the dwarf spheroidal progenitor object. Exceptions include the handful of examples, such as Sagittarius (Belokurov et al. 2006a), Hercules (Coleman et al. 2007), and Ursa Major II (Muñoz et al. 2010), with evidence for tidal stripping. In the tidally stripped satellites, the mass estimates obtained from stellar kinematics provide lower limits on what the central densities of these objects could have been in the past.

The host halos of dwarf spheroidal satellites ostensibly belonging in the common mass scale family should be such frozen-in relics. Their outer dark matter envelopes have long been stripped and their current gravitationally bound masses are substantially reduced compared to the maximum at the point of the tidal truncation of mass assembly. We refer to the maximum mass of the dwarf-hosting halo just before tidal stripping as the maximum tidally truncated mass  $M_{\text{TT}}$  and denote the corresponding redshift with  $z_{\text{TT}} \geq 0$ .

Anticipating our focus on star formation in the dwarf spheroidal progenitor objects below, we note that the cessation of dark matter accretion may be followed with ram pressure stripping of the residual gas in the tidally truncated subhalo (e.g., Mayer et al. 2006), effectively shutting off further star formation. We consider  $z_{\text{TT}}$  an upper limit to the ram pressure stripping redshift  $z_{\text{ram}}$ , the latter being the minimum redshift at which the dwarf formed new stars.

Theoretical expectations for the dark matter halo density pro-

file as a function of mass and redshift in the standard  $\Lambda$ CDM cosmology have been calibrated with cosmological simulations. We assume that the halo density profile is NFW with concentration  $c$  and scale radius  $r_s = r_{200}/c$ , where  $r_{200}$  is the radius at which the mean density inside the halo equals 200 times the critical density of the universe.<sup>1</sup> We adopt the calibration of the halo mass and redshift dependence of the median halo concentration derived by Prada et al. (2012) for halos in the Bolshoi and MultiDark simulations (but see the comments in Ludlow et al. 2012). This parametrization is written in terms of the rms fluctuation  $\sigma(M)$  of the density field linearly extrapolated to  $z = 0$ . In evaluating  $c(M, z)$  at low halo masses, we employ  $\sigma(M)$  computed from the best-fitting Planck Collaboration et al. (2013) cosmological parameter set [from the *Planck* temperature data and *Wilkinson Microwave Anisotropy Probe* (WMAP) polarization] with the help of the CAMB package (Lewis et al. 2000).<sup>2</sup> We find that  $\sigma(M) \approx \sum_{n=0}^3 C_n \log^k(M/M_\odot)$  with  $C_0 = 14.95$ ,  $C_1 = -0.9091$ ,  $C_2 = -0.04806$ , and  $C_3 = 0.003031$  provides an excellent fit in the mass range  $10^5 M_\odot \leq M \leq 10^{12} M_\odot$ .

Halos belonging in a common mass scale family lie on the relation

$$M_{\text{NFW}}[300 \text{ pc}; M_{\text{TT}}, z_{\text{TT}}, c(M_{\text{TT}}, z_{\text{TT}})] = M_{300}, \quad (2)$$

where  $M_{\text{NFW}}(r; M_{\text{halo}}, z, c)$  is the mass enclosed within radius  $r$  for an NFW halo of mass  $M_{\text{halo}}$  at redshift  $z$  having concentration  $c$ . For a specific value of  $M_{300}$ , this defines a one parameter family of halo masses evaluated at the point of the tidal truncation of mass assembly and the corresponding redshifts. Depending on whether we treat the redshift or the mass as an independent variable, we denote this family with

$$M_{\text{TT},\epsilon}(z_{\text{TT}}), \quad z_{\text{TT},\epsilon}(M_{\text{TT}}), \quad (3)$$

where the parameter  $\epsilon$  in the subscript indicates the departure of the  $M_{300}$  parameter from the S08 value

$$\epsilon \equiv \log \left( \frac{M_{300}}{10^7 M_\odot} \right). \quad (4)$$

Note that Equation (2) also defines a maximum halo mass corresponding to  $z_{\text{TT},\epsilon} = 0$  that is consistent with the common mass scale relation. In Figure 1, we show  $z_{\text{TT},\epsilon}(M_{\text{TT}})$  for several representative choices of  $M_{300}$ . For the S08 common mass scale family, solutions with nonnegative tidal redshifts can be found for  $M_{\text{TT},0} \lesssim 1.25 \times 10^9 M_\odot$ , but this upper limit is extremely sensitive to the central density and increases by an order of magnitude to  $M_{\text{TT},+0.3} \lesssim 1.5 \times 10^{10} M_\odot$  after doubling the central density. We find that  $z_{\text{TT},\epsilon}$  increases steeply with decreasing  $M_{\text{TT}}$  until it reaches  $z_{\text{TT},\epsilon} \sim 2$ , and at lower masses and higher redshifts, the redshift increase is more gradual.<sup>3</sup>

<sup>1</sup> The halo density profile is better described with the Einasto profile (e.g., Di Cintio et al. 2013; Vera-Ciro et al. 2013), but the development presented here does not critically depend on the assumed profile.

<sup>2</sup> Equation 12 in Prada et al. (2012) giving the linear growth factor  $D$  is not correctly normalized to unity at  $z = 0$ . We substitute the correctly normalized  $D(a)$  into their Equation 23. Prada et al. (2012) utilize the Klypin et al. (2011) fit to  $\sigma(M)$ , which seems relatively accurate only for  $M > 10^8 M_\odot$ .

<sup>3</sup> The redshifts  $z_{\text{TT},0}$  seem systematically lower than those computed by Macciò et al. (2009) who find  $z_{\text{TT}}(10^8 M_\odot) \sim 7$  and  $z_{\text{TT}}(10^9 M_\odot) \sim 2.5$ . The discrepancy could arise from differences in halo structural properties: derived from relatively coarse resolution cosmological  $N$ -body simulations in Macciò et al. (2009) and from analytical NFW profiles based on the Prada et al. (2012) concentrations in the present work.

Figure 1 further shows that the halo concentrations are approximately independent of the halo mass,  $c \approx 4$ , over most of each common mass scale family, but then increase steeply with increasing mass, to  $c \sim 10$  or higher, near the high-mass end of the common mass scale family, where the corresponding redshifts drop below  $z_{\text{TT},\epsilon} \lesssim 1$ . At these low redshifts, the dimensionless density peak height given by the critical linear overdensity for collapse in units of the  $z = 0$  rms density fluctuation,  $\delta_c(z_{\text{TT},\epsilon})/\sigma(M_{\text{TT},\epsilon})$ , drops below unity, indicating that the massive dwarf spheroidals formed in the collapse of very low- $\sigma$  peaks in the cosmic density field.

The maximum circular velocities of the common mass scale halos, also shown in Figure 1, increase very slowly with  $M_{\text{TT},0}$  and cover the range  $10 \lesssim V_{\text{max}} \lesssim 20 \text{ km s}^{-1}$ . Higher maximum circular velocities of  $V_{\text{max}} \gtrsim 30 \text{ km s}^{-1}$  require  $M_{300} \gtrsim 2 \times 10^7 M_\odot$ . The inability of the S08 common mass scale family to accommodate high  $V_{\text{max}}$  satellite halos is a manifestation of the ‘‘too-big-to-fail’’ problem (Boylan-Kolchin et al. 2011, 2012), which we briefly discuss in Section 6.

## 2.2 The Universal Mass Accretion History of the Common Mass Scale Halos

A crude sense about the formation histories of the common mass scale halos can be obtained by estimating the average masses of the most massive progenitors of halos belonging in the common mass scale one parameter family. Fortunately, accurate approximations describing the halo mass growth rates are available. Fakhouri et al. (2010) measured halo growth rates in the Millennium CDM simulations and obtained a particularly accurate fitting function for mean most massive progenitor histories of halos in the mass range  $10^{10} \leq M_{\text{halo}} \leq 10^{14} M_\odot$ . The fitting function in their Equation 2 can be written in the form

$$\left( \frac{d \ln M_{\text{halo}}}{dz} \right)_{\text{MMP}} \approx -0.62 \left( \frac{1 + 1.11 z}{1 + z} \right) \left( \frac{M_{\text{halo}}}{10^{12} M_\odot} \right)^{0.1}. \quad (5)$$

The cosmological parameters in the Millennium simulations and the Fakhouri et al. (2010) analysis are slightly different from that in the present work, but we nevertheless adopt the redshift dependence of their fitting function, as well as the normalization at the reference mass of  $M_{\text{halo}} = 10^{12} M_\odot$ . Based on the extended Press-Schechter excursion set theory (Lacey & Cole 1993), the mass dependence of the growth rate is set by the linear matter density fluctuation power spectrum and can be approximated via (see, e.g., Neistein et al. 2006)

$$\left( \frac{d \ln M_{\text{halo}}}{dz} \right)_{\text{MMP}} \propto \left| \frac{d\sigma^2(M_{\text{halo}})}{d \ln M_{\text{halo}}} \right|^{-1/2}. \quad (6)$$

The mass dependence of Equation (6) evaluated in the neighborhood of the reference mass  $M_{\text{halo}} = 10^{12} M_\odot$  is  $d \ln |d\sigma^2/d \ln M|^{-1/2}/d \ln M \approx 0.094$ , in good agreement with the mass dependence in Equation (5), but the slope implied by Equation (6) flattens towards lower masses to reach  $d \ln |d\sigma^2/d \ln M|^{-1/2}/d \ln M \approx 0.043$  at  $M_{\text{halo}} = 10^6 M_\odot$ . Therefore, we adopt the mass dependence from Equation (6) to settle on the following form

$$\left( \frac{d \ln M_{\text{halo}}}{dz} \right)_{\text{MMP}} = -0.62 \left( \frac{1 + 1.11 z}{1 + z} \right) \times \left[ \frac{d\sigma^2/d \ln M (M_{\text{halo}})}{d\sigma^2/d \ln M (10^{12} M_\odot)} \right]^{-1/2} \quad (7)$$

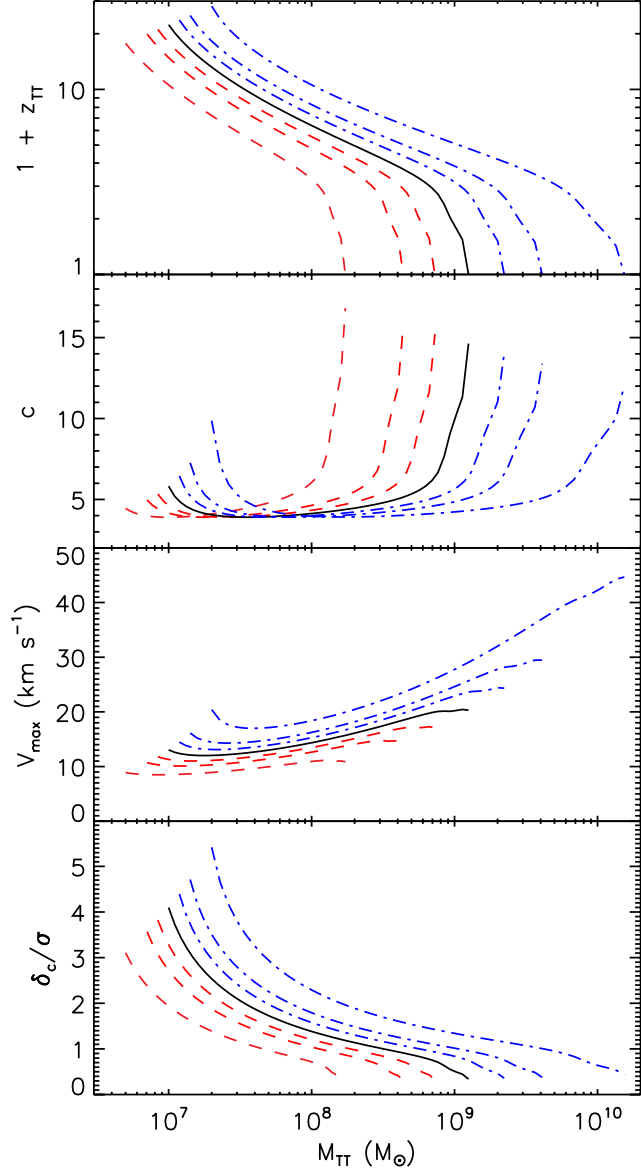


**Figure 1.** Properties of the dark matter halo of mass  $M_{\text{TT},0}$  belonging on the common mass scale relation  $M_{300} = 10^7 M_{\odot}$  at the point at which the external tidal field freezes the evolution of the inner density profile (solid lines). The panels from top to bottom show the redshift  $z_{\text{TT},0}(M)$ , the corresponding halo concentration  $c$ , maximum circular velocity of the halo  $V_{\text{max}}$ , and overdensity peak height in units of the rms density variance  $\delta_c(z)/\sigma(M)$ . The dashed and dot-dashed lines show the neighboring common mass scale relations as a function of  $M_{\text{TT},\epsilon}$  for  $M_{300} = (2^{-1}, 2^{-0.5}, 2^{-0.25}) \times 10^7$  and  $(2^{0.25}, 2^{0.5}, 2^1) \times 10^7 M_{\odot}$ , respectively.

Integrating Equation (7) we compute the mean most massive progenitor histories for halos belonging in the common mass scale family which we denote with

$$M_{\text{MMP}}[M_{\text{TT}}, z_{\text{TT},0}(M_{\text{TT}}); z]. \quad (8)$$

A sample of representative histories for two common mass scale families,  $M_{300} = 10^7$  and  $2 \times 10^7 M_{\odot}$ , is shown in Figure 2. We find that the histories have a very weak dependence on  $M_{\text{TT}}$  at a fixed redshift  $z$ , with the variation being particularly small for the S08 family. The common mass scale halos in the S08 family have

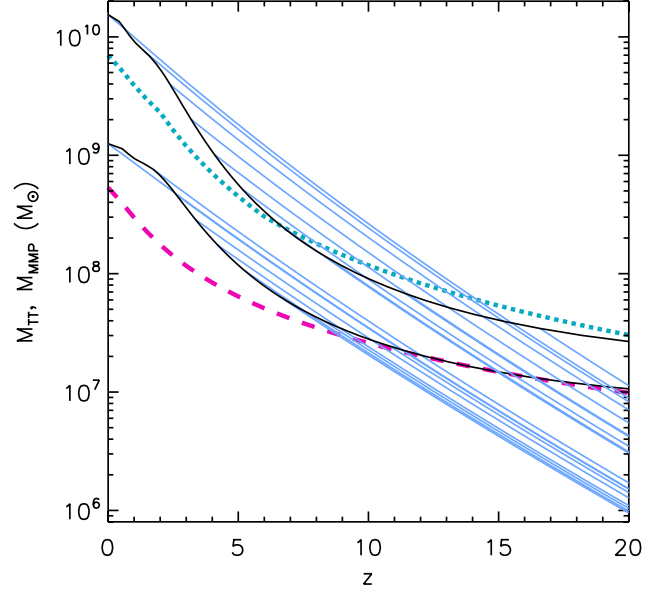


**Figure 2.** Mass of the halos in the common mass scale family as a function of redshift  $M_{\text{TT},\epsilon}(z)$  for  $M_{300} = 10^7 M_{\odot}$  (lower black curve) and  $M_{300} = 2 \times 10^7 M_{\odot}$  (upper black curve). The curves in light blue show representative most massive progenitor histories of the halos in the two common mass scale families. The thick dashed magenta line and the thick dotted cyan line show the halo masses corresponding to  $T_{200} = 10^4$  K (assuming neutral gas,  $\mu_{\text{mol}} = 1.22$ ) and  $T_{200} = T_{200,\text{crit}}(z)$  (assuming ionized gas,  $\mu_{\text{mol}} = 0.6$ ) respectively (see Section 3.2).

similar mean accretion histories, at any given redshift varying over less than a factor of 2 in mass. This can be understood as reflecting the fact that the dense material in the center of a halo is put in place early on, only to evolve passively as the mass and virial radius of the halo grow by accreting from a universe of a progressively decreasing density. The central densities of the most massive progenitor halos evolve very little with redshift up to some maximum redshift at which an active assembly of what is to become the dense central core of the halo is taking place. This is consistent with the behavior seen in Figure 1 in which the concentrations of halos with maximum tidally limited masses  $M_{\text{TT},0} \lesssim 10^8 M_{\odot}$  are  $c \approx 4$ , approximately independent of the mass, but at the highest halo masses, they increase sharply with the increasing mass.

The universal history of the common mass scale halos is already apparent in the conclusion of Wolf et al. (2010) that the dwarf spheroidal satellites of the Milky Way, if they were to be artificially placed into *isolated* halos at  $z = 0$  as required to match their stellar dynamical central density estimates, would all reside in similar mass halos  $M_{\text{iso},z=0} \sim 3 \times 10^9 M_{\odot}$ . This formal conclusion is consistent within uncertainties with our estimate of the  $z_{\text{TT},0} = 0$  common mass scale halo mass. Nevertheless, given that the tidal truncation redshifts will vary across the dwarf spheroidal satellite sequence, and so will the average halo densities and concentrations, the physical significance of the  $z = 0$  isolated-halo-equivalent masses of Wolf et al. (2010) is not entirely clear.

### 2.3 Satellite Inspiral Times

After a satellite halo becomes incorporated in the substructure of one of the massive progenitors of the Milky Way or Andromeda, dynamical friction drives its orbit to decay. For the subhalo to be

observed as a satellite galaxy at  $z = 0$ , the orbital decay time must be longer than the time elapsed since the infall. The orbital decay time depends on the masses and concentrations of the two halos and on the parameters of the orbit. Here, we adopt a crude, order-of-magnitude estimate of the orbital decay time (see, e.g., Cooray & Milosavljević 2005),

$$\tau_{\text{DF}} \sim \xi \tau_{\text{ff}} \frac{M_{\text{host}}}{M_{\text{sat}}}, \quad (9)$$

where  $\xi$  is a dimensionless coefficient likely to lie in the range  $0.1 - 1$ ,  $\tau_{\text{ff}} \sim [3\pi/(32 G \bar{\rho}_{\text{host,sat}})]^{1/2} \approx 0.1 H(z)^{-1}$  is the free fall time of the halos,  $\bar{\rho}_{\text{host,sat}} = 200 \times 3H(z)^2/(8\pi G)$  is the average density of the halos,  $H(z)$  is the Hubble parameter at redshift  $z$ , and the host and satellite halo masses can be set to

$$\begin{aligned} M_{\text{host}} &= M_{\text{MMP}}[M_{\text{MW}}, 0; z_{\text{TT},0}(M_{\text{TT}})], \\ M_{\text{sat}} &= M_{\text{TT}}. \end{aligned} \quad (10)$$

The most massive progenitors of a Milky Way-like halo with a mass of  $10^{12} M_{\odot}$  at  $z = 0$  had average masses  $\log(M_{\text{MMP,MW}}/M_{\odot}) = (11.7, 10.7, 9.7)$  at redshifts  $z = (1, 5, 10)$ , respectively, in agreement with Figure 6 of Fakhouri et al. (2010). For the same redshifts, we have  $\log(M_{\text{TT},0}/M_{\odot}) \approx (9, 8, 7.3)$ . This shows that  $M_{\text{host}}/M_{\text{sub}} \sim 500$  for  $M_{\text{TT},0} \gtrsim 10^8 M_{\odot}$  and the ratio then gradually declines towards lower masses and higher infall redshifts. Comparing the orbital decay time to the Hubble time, we find

$$\tau_{\text{DF}} H_0 \sim \xi \frac{50}{H(z)/H_0} \frac{M_{\text{host}}/M_{\text{sat}}}{500}. \quad (11)$$

The value of  $\xi$  must be constrained with high-resolution cosmological simulations. For example, for  $\xi \sim 0.2$ , the orbital decay time is longer than the Hubble time,  $\tau_{\text{DF}} H_0 > 1$ , for halos of the S08 common mass scale family with  $z_{\text{TT},0} \lesssim 6$ . This is sufficient to guarantee that a significant fraction of the S08 family progenitor objects will not have inspiralled too close to the Galactic Center and thus been completely disrupted. For the  $M_{300} = 2 \times 10^7 M_{\odot}$  family, the maximum redshift for avoiding orbital decay drops to  $z_{\text{TT},+0.3} \lesssim 5$  (corresponding to  $M_{\text{TT},+0.3} \gtrsim 5 \times 10^8 M_{\odot}$ ), implying that low-mass halos in the latter family will have been lost to the Galactic Center.

### 3 REIONIZATION AND BARYONIC CONTENT

#### 3.1 Dwarf Spheroidal Progenitors at Reionization

It is widely considered that cosmic reionization defined the properties of the dwarf spheroidal galaxy population in the Local Group, but the details of its role vary in the rich literature on this subject (e.g., Bullock et al. 2000; Benson et al. 2002; Grebel & Gallagher 2004; Kuposov et al. 2009; Muñoz et al. 2009; Okamoto & Frenk 2009; Busha et al. 2010; Macciò et al. 2010; Font et al. 2011; Lunnan et al. 2012). The objects that formed before reionization has swept through their local protogalactic patches are sometimes called “fossils” (e.g., Ricotti & Gnedin 2005; Gnedin & Kravtsov 2006). The more luminous, “classical” dwarfs in the Local Group contain stellar populations spanning a wide range of stellar ages and are not fossils. The ultra-faint dwarfs, however, are typically old (e.g., Brown et al. 2012, and references therein), and, from the standpoint of their stellar ages and the statistics of their radial distances from the center of their Local Group host galaxy, are consistent with being fossils (e.g., Bovill & Ricotti 2009, 2011a,b; Muñoz et al. 2009; Salvadori & Ferrara 2009; Frebel & Bromm 2012).

It is striking that the ultra-faint and classical dwarfs seem to

form a single, one-dimensional sequence in the luminosity-radius-metallicity space (see, e.g., Belokurov et al. 2007; Gilmore et al. 2007; Tolstoy et al. 2009; Wolf et al. 2010; Kirby et al. 2011a; Misgeld & Hilker 2011; Kormendy & Bender 2012; McConnachie 2012), in addition to having similar central mass densities. The latter property, of course, places them on the reported common mass scale relation. This continuity of properties raises the prospect of *formation under uniform conditions across the entire dwarf spheroidal satellite sequence*. Reionization modifies these conditions drastically; therefore, it is worth comparing the dwarfs’ observed properties to theoretical expectations for the properties of galaxies forming under completely reionized conditions. We proceed with this exercise, leaving the question of the nature and manifestation in the Local Group of the true pre-reionization fossils to a brief discussion in Section 6.

What were the typical masses of the most massive progenitors of the dwarf spheroidal satellite host halos at redshifts at which the Local Group could have plausibly undergone reionization? For the common mass scale halos in the S08 family, as Figure 2 shows, we find  $M_{\text{MMP}} \sim 10^7 M_{\odot}$  at  $z \sim 12 - 14$  and  $M_{\text{MMP}} \sim 10^8 M_{\odot}$  at  $z \sim 5 - 7$ . The reference masses selected here bracket the range of the halo masses, known as the “atomically cooling halos,” in which the baryons are first becoming able to cool by the collisionally excited  $\text{Ly}\alpha$  line emission (e.g., Oh & Haiman 2002; Bromm & Yoshida 2011). The corresponding redshifts are low compared to those of the first, Population III stars to form in the Local Group, and bracket the range of redshifts at which reionization of the Local Group volume is generally expected (e.g., Li et al. 2013; Ocvirk et al. 2013). The global reionization redshift of the universe as inferred from the analysis of cosmic microwave background (CMB) anisotropy by artificially fixing the reionization width to  $\Delta z = 0.5$  is  $z_{\text{reion}} = 11.1 \pm 1.1$  (Planck Collaboration et al. 2013, the limits from *Planck* temperature data and *WMAP* polarization at low multipoles), also belongs in this redshift range.

The very first stars in the Milky Way already formed at redshifts  $\lesssim 35$  in halos with masses  $\gtrsim 10^5 M_{\odot}$  (e.g., Gao et al. 2010). As Figure 2 shows, however, the mean most massive progenitors of the common mass scale objects crossed the threshold for  $\text{H}_2$  cooling, which enables metal-free star formation, at redshifts  $\lesssim 20$  and at halo masses  $\gtrsim 10^6 M_{\odot}$  (e.g., O’Shea & Norman 2007). At these redshifts, the critical halo mass for star formation will have possibly been substantially increased by a growing  $\text{H}_2$ -molecule-dissociating (Lyman-Werner) background (e.g., Johnson et al. 2008; Ahn et al. 2009; Holzbauer & Furlanetto 2012; Fialkov et al. 2013). At redshifts  $z_{\text{LW}} \sim 15 - 20$ , this background will have raised the minimum mass of metal-free halos capable of forming stars to a threshold  $M_{\text{crit,LW}} \gtrsim 10^7 M_{\odot}$  at which the  $\text{Ly}\alpha$  line cooling allows the gas to start collapsing to densities at which self-shielding from the dissociating radiation becomes effective (e.g., O’Shea & Norman 2008; Wolcott-Green et al. 2011; Safranek-Shrader et al. 2012). The common mass scale objects’ most massive progenitors will have crossed  $M_{\text{crit,LW}}$  at redshifts at which the Local Group will have already begun to become reionized.

All this suggests that the dwarf spheroidal progenitor objects should have largely avoided forming stars before reionization. Some may had been able to form a few stellar generations before becoming affected by the UV backgrounds, e.g., in the aftermath of a prompt enrichment by supernovae (SNe) from moderate-mass Pop III stars (Ritter et al. 2012), but others would have found themselves starless at the brink of reionization. This is consistent with the continuity of structural and chemical properties identified above. We note that Kuposov et al. (2009), who modeled the Milky

Way satellite population with various prescriptions for baryonic mass reduction after reionization and baryon-to-star conversion efficiencies, had previously arrived at the same conclusion, that the best-fitting models require that the bulk of the stars formed after reionization.

One useful simplification is to encapsulate the impact of the ionizing background into a single variable, the baryon fraction  $f_b$ , which will normally be limited from above by the cosmic mean  $\Omega_b/\Omega_m$ . After a patch of the universe has been reionized and the baryons in small halos in the patch photoevaporated (Barkana & Loeb 1999; Shapiro et al. 2004), the baryon fraction, and with it the threshold for star formation, is modulated by the thermodynamics of the photoionized intergalactic medium (IGM) and the relative strength of the gravitational and pressure forces during halo assembly, as well as by the competition of ionization and recombination in the densest gas located near the center of the halo (e.g., Thoul & Weinberg 1996; Kepner et al. 1997; Kitayama & Ikeuchi 2000; Kitayama et al. 2000, 2001; Dijkstra et al. 2004; Susa & Umemura 2004; Mesinger & Dijkstra 2008; Sobacchi & Mesinger 2013a). The pressure force resists the dark matter's gravitational pull already at the turnaround point of the gravitational collapse and thus acts to reduce the baryon mass fraction in virialized dark matter halos. The pressure is determined by the thermodynamic evolution of the gas, which is itself a function of the detailed history of halo mass assembly, of the chemistry of the gas, and of the character of UV and X-ray radiation backgrounds. The interplay of these factors renders the problem of determining the threshold for runaway baryonic collapse in reionized halos complex and best addressed with cosmological hydrodynamic simulations (e.g., Gnedin 2000, 2012; Hoeft et al. 2006; Okamoto et al. 2008). We proceed to model the baryon fraction of the dwarf spheroidal progenitor halos aided with the results of these numerical investigations.

### 3.2 Baryon Fractions

The principal structural property of a halo determining its baryon fraction is the depth of the gravitational potential well, which can be quantified with a characteristic velocity or (virial) temperature. The velocity or temperature can be compared to the values required for baryon retention in halos exposed to an ionizing background of a given intensity. A number of investigations have sought to calibrate the dependence of the baryon fraction on halo properties and the reionization history. Okamoto et al. (2008, hereafter O08) measured the baryon fraction in cosmological gas dynamical simulations of halo collapse in a section of the universe undergoing reionization, and found that the characteristic virial temperature  $T_{\text{vir,crit}}$  for a halo to retain half of its universal allotment of baryons is approximately independent of redshift  $T_{\text{vir,crit}} \approx 2 \times 10^4$  K at low redshifts  $z \lesssim 2$  and decreases steeply with increasing redshift at  $z > 2$ . The steep drop is a consequence of the finite time, of the order of the sound crossing time in the photoionized gas, that it takes gas to escape the host halos upon reionization, and also a consequence of the retention of dense gas in infalling subhalos with deep potential wells (T. Okamoto, priv. comm.). We expect that the critical virial temperatures would have been higher than those estimated by O08 had unbound gas been excluded in the computation of baryon fractions. O08 neglected radiative transfer effects such as self-shielding which could have had the opposite effect.

Sobacchi & Mesinger (2013a, hereafter SM13a) carried out spherically symmetric simulations of baryonic collapse in halos before the completion of reionization, at  $z \geq 6$ , and computed the critical halo masses  $M_{\text{crit}}$  for retaining half of the baryons,

but now excluding any unvirialized or unbound gas. The resulting masses are systematically higher than the corresponding masses in O08, perhaps a consequence of the more selective criterion for tallying the virialized baryons in SM13a, but the redshift dependence is similar, again corresponding to a  $T_{\text{vir,crit}}$  that decreases with redshift. SM13a fit the critical mass in fully reionized halos to find a scaling

$$M_{\text{crit}} \propto J_{\text{ion}}^{0.17} (1+z)^{-2.1}, \quad (12)$$

where  $J_{\text{ion}}$  is the mean intensity of the ionizing background. This fit was calibrated at  $z \geq 6$  but we extrapolate it to lower redshifts, where both UV and X-ray photons contribute to the ionizations. The UV dominates until  $z \sim 3$  and X-rays at lower redshifts. Expressed in terms of the hydrogen photoionization rate  $\Gamma_{\text{HI}}$ , the background intensity has been measured to rise gradually from  $z \sim 6$  to  $z \sim 5$  to a steady maximum level of  $\Gamma_{\text{HI}} \sim 10^{-12} \text{ s}^{-1}$  (Becker & Bolton 2013). Then, after the peak of quasar activity at  $z \sim 2$ , the photoionization rate declines sharply, by a factor of  $\gtrsim 10$  by  $z = 0$  (Haardt & Madau 2012, and references therein).

It is not clear if the low-redshift drop in  $J_{\text{ion}}$  should translate into a reinvigorated infall of baryons into isolated dwarf galaxy halos and whether that would lead to a corresponding decrease in  $M_{\text{crit}}$ . If some reinvigorated infall does happen before the tidal truncation of mass assembly, that could give rise to renewed star formation in dwarf spheroidal progenitor objects (e.g., Ikeuchi et al. 1989; Babul & Rees 1992; Ricotti 2009). However, this effect does not seem to be manifest in the results of O08. The reinvigorated infall may not be taking place because it takes a finite time, similar to the Hubble time, for the baryons to cool and fall back into the halos (Noh & McQuinn 2014), especially given that additional hydrodynamic effects (shocks and bulk flows; Mo et al. 2005; Benítez-Llambay et al. 2013) associated with the collapse of long-wavelength large scale structure modes are stirring and raising the entropy of the IGM at the relevant redshifts and mass scales. For this reason, we assume in agreement with O08 that  $T_{\text{vir,crit}}$  is a constant or monotonically decreasing function of  $z$ , not exhibiting a drop towards low redshifts that would be naively expected from a falling  $J_{\text{ion}}$ .

Before the completion of reionization, at  $z > 6$ , the globally averaged ionizing background intensity is expected to decline with redshift with the decrease of the ionized volume fraction. The local intensity inside cosmic H II regions, on the other hand, will exhibit little evolution with redshift (e.g., Sobacchi & Mesinger 2013b, where in H II regions, the ionization rate is approximately constant,  $\Gamma_{\text{HI}} \sim (2-4) \times 10^{-13} \text{ s}^{-1}$  over the redshift interval  $7 < z < 15$ ). In view of our hypothesis that the dwarf spheroidal progenitor objects in the Local Group formed in reionized patches, we adopt the latter photoionization rate for  $z > 6$ .

Given these considerations, we construct a model for  $M_{\text{crit}}(z)$  as follows. First, we choose the  $z = 0$  values of  $M_{\text{crit}}$  and

$$T_{200,\text{crit}} = \frac{\frac{1}{2} \mu_{\text{mol}} m_p G M_{\text{crit}}}{k_B r_{200,\text{crit}}}, \quad (13)$$

where  $\mu_{\text{mol}} \approx 0.6$  is the mean molecular weight in units of the particle mass in ionized gas, to equal those reported by Gnedin (2012) and consistent with O08,

$$M_{\text{crit}}(0) = 7 \times 10^9 M_{\odot}, \quad T_{200,\text{crit}}(0) = 2.8 \times 10^4 \text{ K}. \quad (14)$$

Then, as in O08, we assume that at  $z < 2$ , the  $M_{\text{crit}}$  halos have redshift-independent virial temperatures. At redshifts  $2 < z < 6$ , we utilize the scaling in Equation (12) with an effective ionizing background (incorporating both the UV and X-ray contributions)

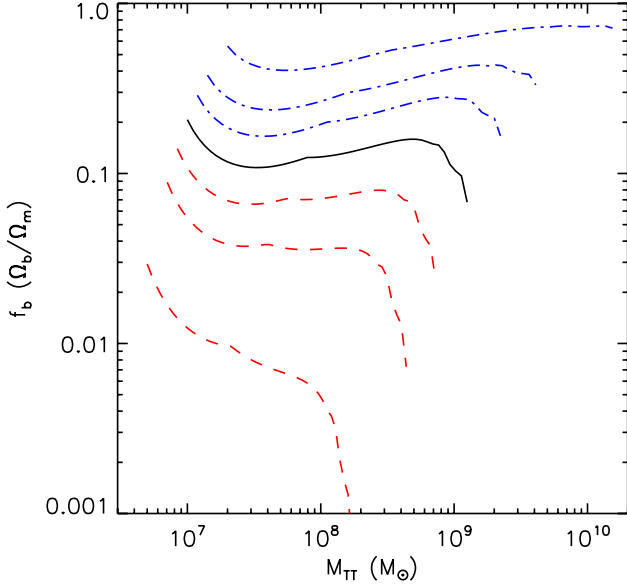


**Figure 3.** The baryon fraction in units of the universal baryon fraction  $(\Omega_b/\Omega_m)^{-1}$  at the point at which the external tidal field freezes the evolution of the inner density profile (black solid line). The red, dashed and blue, dot-dashed lines show the neighboring common mass scale relations for  $M_{300} = (2^{-1}, 2^{-0.5}, 2^{-0.25})$  and  $(2^{0.25}, 2^{0.5}, 2^1) \times 10^7 M_\odot$ , respectively.

that decreases exponentially in  $z$  by a factor of 3 over this redshift range. At redshifts  $z > 6$ , we continue applying Equation (12), but we assume that the ionizing background parameter  $J_{\text{crit}}$  in ionized patches is constant. Since for  $z > 2$ ,  $T_{200} \propto M_{\text{halo}}^{2/3} (1+z)$  is a good approximation, we have

$$\frac{T_{200,\text{crit}}(z)}{T_{200,\text{crit}}(0)} = \begin{cases} 1 & , z < 2, \\ 3^{-0.17(z-2)/4} [(1+z)/3]^{-0.4} & , 2 < z < 6, \\ 3^{-0.17[(1+z)/3]^{-0.4}} & , z > 6. \end{cases} \quad (15)$$

It remains to model how, at a given redshift, the baryon fraction  $f_b(M_{\text{halo}}, z)$  varies with  $M_{\text{halo}}$  such that  $f_b(M_{\text{crit}}, z) = \frac{1}{2} \Omega_b/\Omega_m$ . Several models describing the variation of the baryon fraction with the ratio of the halo mass to the critical mass  $M_{\text{halo}}/M_{\text{crit}}(z)$ , but otherwise having no explicit dependence on redshift, exist in the literature. We utilize the Gnedin (2000) form

$$f_b(M_{\text{halo}}, z) \approx \frac{\Omega_b}{\Omega_m} \left\{ 1 + (2^{\alpha/3} - 1) \left[ \frac{M_{\text{halo}}}{M_{\text{crit}}(z)} \right]^{-\alpha} \right\}^{-3/\alpha}, \quad (16)$$

where  $\alpha$  is a shape parameter.<sup>4</sup> O08 report a good fit with  $\alpha = 2$ , whereas Gnedin (2012), who has also measured the baryon fraction in cosmological simulations, reports  $\alpha = 1$ . The two choices of  $\alpha$  imply substantial differences for  $M_{\text{halo}} \sim M_{\text{crit}}$  but both scale as  $f_b \propto M_{\text{halo}}^{-3}$  for  $M_{\text{halo}} \ll M_{\text{crit}}$ . We adopt the Gnedin (2012) functional form with  $\alpha = 1$  since SM13a agree that it fits their data.

<sup>4</sup> SM13a adopt a simpler functional dependence:

$$f_b(M_{\text{halo}}, z) \approx \frac{\Omega_b}{\Omega_m} \frac{e^{-M_{\text{halo}}/M_{\text{crit}}(z)+1}}{2}. \quad (17)$$

In Figure 3, we show the baryon fractions of the common mass scale halos at the point of the tidal truncation of mass assembly. They are approximately independent of the halo mass and are all substantially below the cosmic mean,  $f_b \sim (0.1 - 0.15) \Omega_b/\Omega_m$ . The small variation of  $f_b$  with  $M_{\text{TT},\epsilon}$  seen in Figure 3 is not significant in view of the various model uncertainties.<sup>5</sup> The scaling of the baryon fraction with a single parameter,  $M_{300}$ , if not a modeling coincidence, seems interesting in itself, perhaps suggesting that it is the free fall time of the inner halo (which is directly related to the density and thus to  $M_{300}$ ) that determines the degree of reionization-induced baryonic infall suppression.

Because of the steep decrease of the baryon fraction with decreasing halo mass at a fixed redshift, it is clear that any halos that are less dense in their central 300 pc than the common mass scale halos would have great difficulty retaining even a small fraction of their universal allotment of baryons and, consequently, would not be expected to form any stars. One may thus be tempted to conclude that the common mass scale is shaped by the influence of reionization: halos that are denser than those on the common mass scale entered a rapid star formation mode before reionization and leave behind stellar systems that would not be recognized as dwarf spheroidals—the ultra-faint and classical dwarfs—in the Local Group. We speculatively revisit the question of the nature of pre-reionization fossils in Section 6 below. On the other hand, objects that are less dense than those on the common mass scale retained too small a fraction of their baryons to form stars, and remained dark (see also Section 4.2.5 below, where we find that gas in the dwarfs with  $M_{300} \lesssim 5 \times 10^6 M_\odot$  may remain in the ionized phase).

Other processes may additionally influence the baryon fraction in low-mass halos, such as gas heating (Mo et al. 2005, however, see Crain et al. 2007) and ram pressure stripping (Benítez-Llambay et al. 2013) by shock waves and flows produced by the collapsing large-scale structure, as well as the expulsion of baryons by the feedback from star formation in the host halo (e.g., Okamoto et al. 2010; Font et al. 2011). The efficiency and statistics of these processes are still highly uncertain. Additional sources of theoretical uncertainty that are particularly challenging to remove, even with the best currently available cosmological hydrodynamical simulations, include the transport of nucleosynthetic products from their progenitor stars (including the very first, Population III) which directly affects the thermodynamic evolution of star-forming gas, and the potential survival of compact, dense, pressure-confined clouds in the face of the disruption by reionization and star formation feedback. Our intention here is to develop a minimal model for the formation of the dwarf spheroidal satellite population in the Local Group, and thus we do not attempt to characterize the impact of these processes.

## 4 STAR FORMATION

### 4.1 How Did Dwarf Spheroidal Satellites Form Their Stars?

We turn to modeling star formation in the dwarf spheroidal progenitors. First clues about the character of the gas flows that formed the bulk of the stars can be obtained from the galaxy structural properties. The dwarf spheroidal satellite stellar systems form a

<sup>5</sup> The baryon fractions are somewhat larger than the values  $f_b \sim (0.01 - 0.05) \Omega_b/\Omega_m$  found by Simpson et al. (2013) in cosmological simulations modeling the formation of dwarf spheroidal satellite-like galaxies.

one-dimensional family in the luminosity-effective radius or stellar mass-effective radius plane (Belokurov et al. 2007; Gilmore et al. 2007; Tolstoy et al. 2009; Wolf et al. 2010; Kirby et al. 2011a; Misgeld & Hilker 2011; Kormendy & Bender 2012; McConnachie 2012). The family is well separated from the families occupied by the more concentrated globular clusters, ultra-compact dwarfs, and dwarf elliptical galaxies (M32), but connects smoothly with the family of spheroidal galaxies (Kormendy et al. 2009). Excluding the stellar nuclei that are ubiquitous in the comparatively luminous spheroidals (e.g., Côté et al. 2006), and are seen in Sagittarius and NGC 205 in the Local Group, surface brightness profiles of the entire spheroidal family have low Sérsic-indices  $n \sim 1 - 2$ , similar to the index of the exponential disk  $n = 1$ .

The relation defined by the dwarf spheroidals’ stellar masses and effective radii also agrees with that of the galaxy disks (e.g., Figure 13 of Gadotti 2009) and of the disk-like, low-luminosity dwarf irregular galaxies in the range of stellar masses where the two morphological types overlap (see, e.g., Kormendy & Bender 2012). The luminosity- (or stellar mass-) metallicity relation for dwarf irregulars also coincides with that for dwarf spheroidals (Kirby et al. 2013). The average star formation histories of the two populations and of the intermediate “transition dwarf” population also form a continuum (Weisz et al. 2011). The disks themselves are well described with the exponential surface brightness profile. The structural similarity between the two populations seems to suggest a disk-like origin for the dwarf spheroidals, in the sense that the gas in which the stars formed was, as in disks, rotationally supported and endowed with an angular momentum distribution that would produce an exponential surface density profile. The observation that the lowest-luminosity galaxies in group and cluster environments and in the field are almost exclusively spheroidal and dwarf irregular, respectively (A. Klypin, priv. comm.), further supports the galaxy transformation paradigm (e.g., Grebel et al. 2003) in which the lowest mass galaxies transition through the star-forming, dwarf irregular form before getting accreted on to a more massive system and stripped of the gas.

The disk-like gas flows, which we will argue have produced the dwarf spheroidal satellites in the Local Group, can be contrasted with the unstable, disordered flows seen in galaxy mergers and in systems containing high-accretion-rate, high-Mach-number baryonic inflows (sometimes called “cold-mode” accretion). The disordered flows are expected and observed to exhibit rapid gas transport into the central region or pervasive, large-scale clumping. It is believed that disordered flows produce more concentrated central stellar components similar to the stellar bulges and nuclear clusters in disk galaxies and stellar density cusps in ellipticals (Hopkins et al. 2009). Disordered flows arise when gas is globally self-gravitating, or is flowing into the galaxy with highly supersonic velocities, or has somehow lost much of its angular momentum, e.g., in the fluctuating gravitational field of a galaxy merger.

The dwarf spheroidal progenitor objects, if forming in a reionized patch of the universe, do not seem to fulfill the conditions for the development of violently disordered flows. Their reduced baryon fractions imply that the gas condensing in these halos is unlikely to have been globally self-gravitating; the baryons settle in rotating hydrostatic quasi-equilibria dominated by dark matter gravity. Their analogs among the field galaxies in the nearby universe are the HI-rich (typically “irregular”) dwarf galaxies (e.g., Begum et al. 2006; Roychowdhury et al. 2010; Cannon et al. 2011; Papastergis et al. 2011; Huang et al. 2012), which exhibit varying degrees of rotational and pressure support and very little or no evidence for molecular gas. The paucity of molecular gas is consistent

with the dwarf galaxies having relatively low total gas surface densities, below the limit for efficient atomic-to-molecular conversion.

Our picture is that the dwarf spheroidal progenitor objects formed the bulk of their stars over extended periods in partially rotationally supported, globally gravitationally stable neutral gas flows, which we will refer to as “disks.” In halos hosting such disks, continued gas accretion from the cosmic web could induce directional drift of the angular momentum axis of the disk. Stars would inherit the instantaneous sense of rotation of the gas flow at the time of formation, and this sense could evolve over time. Collisionless dynamical processes, such as the tidal stirring during the infall of the dwarf galaxy into a more massive halo (e.g., Mayer et al. 2001a,b; Kazantzidis et al. 2011), might further modify the stellar orbital structure and erase coherent rotation. The resulting stellar systems forming from disk-like flows would no longer have disk-like kinematics; they might in fact end up “dynamically hot,” consistent with the spheroidal classification.

We will assume that similar to the low-redshift HI disks in the spirals (e.g., Swaters et al. 2002) and dwarf irregulars (e.g., Hunter et al. 2011), the dwarf spheroidal progenitor disks had exponential gas surface density radial profiles. A corpus of observational and theoretical investigations of star formation has isolated the gas column density and metallicity as the primary parameters controlling the star formation rate. At column densities above a threshold of  $\gtrsim 10 M_{\odot} \text{pc}^{-2}$  at metallicities  $Z \sim Z_{\odot}$  and potentially higher thresholds at  $Z \ll Z_{\odot}$ , the disk gas is predominantly in the molecular phase; at lower column densities, it is primarily atomic. We will find that reduced baryon fractions (Section 3.2) will imply relatively low total gas column densities in the dwarf spheroidal progenitor disks, suggesting predominantly atomic gas.

Many of the details of star formation in the regime in which HI dominates the chemical state of the gas remain to be understood, but some trends are emerging from recent work. The heating and cooling processes in the gas should be strong functions of metallicity, but the net effect of the metallicity on gas thermodynamics may involve competing influences that partially cancel each other (see, e.g., Krumholz et al. 2011; Glover & Clark 2012a,b). The heating at typical densities characteristic of the warm neutral medium (WNM) to cold neutral medium (CNM) transition, which is itself driven by the thermal instability (e.g., Saury et al. 2013, and references therein), is facilitated by the photoelectric effect on dust grains. The dust abundance increases with metallicity, as does the ability of the gas to shield itself from the interstellar radiation field. At low metallicities and reduced molecule abundances, the cooling by atomic fine structure lines at low densities and dust at high densities dominates over molecular cooling. While the star formation rate clearly correlates with the  $\text{H}_2$  abundance inferred from CO observations (e.g., Schrubba et al. 2011), the molecules in the atomically dominated regime can be thought of as a tracer of the star-forming CNM (e.g., Krumholz et al. 2011; Krumholz 2012).

The average stellar metallicities of the dwarf spheroidals are low, e.g.,  $-2.6 \lesssim \langle [\text{Fe}/\text{H}] \rangle \lesssim -1$  (Kirby et al. 2011a), and these are lower metallicities than the ones for which star formation rates as a function of HI and  $\text{H}_2$  column densities have been calibrated with  $\text{H}\alpha$  and far-ultraviolet (FUV) observations in the nearby universe. Theoretical star formation prescriptions that utilize the linear relation between the  $\text{H}_2$  and star formation rate surface densities (e.g., Krumholz & Dekel 2012; Kuhlen et al. 2012, 2013) are likewise not valid at metallicities as low as found in the dwarf spheroidals, where they would predict complete absence of star formation (see, e.g., the discussion in Kuhlen et al. 2013, where an artificial floor on the  $\text{H}_2$  abundance is imposed). We do not attempt to

construct a theoretical model for the star formation rates, but turn to the local dwarf irregular galaxies for clues about the efficiency with which the dwarf spheroidal progenitor objects formed their stars.

A number of measurements of star formation rates at low column densities and low metallicities based on H $\alpha$  and FUV fluxes in the nearby dwarf irregulars (e.g., Begum et al. 2008; Roychowdhury et al. 2010, 2011) are consistent with the time-scales for HI depletion by star formation  $\tau_{\text{dep,irr}} = \Sigma_{\text{HI}}/\Sigma_{\text{SFR}} \sim 10$  Gyr. Other measurements agree with or potentially exceed this scale. van Zee (2001) measured an average depletion time-scale of  $\tau_{\text{dep,irr}} \sim 20$  Gyr in a sample of dwarf irregular galaxies. The conditions in dwarf irregular gas disks (surface densities, metallicities, tidal field strengths) are approximately mimicked in the outer disks of more massive disk galaxies. Bigiel et al. (2010) carried out FUV measurements of the star formation rates in the outer disks of the nearby disk galaxies and found gas depletion time-scales ranging from  $\tau_{\text{dep,edge}} \sim 100$  Gyr at  $\Sigma_{\text{HI}} \sim 1 M_{\odot} \text{pc}^{-1}$  to  $\tau_{\text{dep,edge}} \sim (10 - 30)$  Gyr at  $\Sigma_{\text{HI}} \sim 10 M_{\odot} \text{pc}^{-1}$ . Hunter et al. (2011) find a similar trend examining the outer edges of five dwarf irregulars. At higher surface densities, the depletion times drop below 10 Gyr (Schruba et al. 2011). In view of these empirical constraints, we adopt the time-scale for HI-to-stars conversion of

$$\tau_{\text{dep}} = \frac{M_{\text{HI}}}{\dot{M}_{\star}} \sim 10 \text{ Gyr} \quad (18)$$

as the star formation time-scale in the dwarf spheroidal progenitor objects.<sup>6</sup>

## 4.2 Gas Disks in Dwarf Spheroidal Progenitors

### 4.2.1 Surface Densities

Our approach to modeling the gas disks in the dwarf spheroidal progenitor objects is based on the standard methods (e.g., Mo et al. 1998; Schaye 2004; Dekel et al. 2013). We assume that the radial dependence of the baryon surface density in the collapsed component is exponential

$$\Sigma(R) = \Sigma_0 e^{-R/R_{\text{disk}}}, \quad (19)$$

consistent with the ubiquity of the exponential profile in outer HI disks in nearby galaxies (e.g., Swaters et al. 2002; Hunter et al. 2011). Here,  $R_{\text{disk}}$  denotes the characteristic disk exponential scalelength, which can be written in terms of the dimensionless baryonic spin parameter  $\lambda$  via

$$R_{\text{disk}} = \frac{\lambda r_{200}}{\sqrt{2}}. \quad (20)$$

We take this relation, rather than the usual one expressing the angular momentum of the disk in terms of that of the halo, to define  $\lambda$ . While  $\lambda$  is set by the linear and non-linear torques during gravitational clustering and hydrodynamical evolution and varies

<sup>6</sup> This depletion time is a factor of  $\sim 5-10$  shorter than the depletion times estimated by Kuhlen et al. (2013) for halos of mass  $M_{\text{halo}} \lesssim 10^{10} M_{\odot}$  at  $z = 2.5$ . The success of our choice of  $\tau_{\text{dep}}$  in explaining the dwarf spheroidal population of the Local Group (see Section 5 below) suggests that reconciling the longer  $\tau_{\text{dep}}$  of Kuhlen et al. (2013) with the observed luminosity-radius relation would require an evolutionary reduction of the dark matter density as quantified by  $M_{300}$ , e.g., by baryonic processes (see, e.g., Arraki et al. 2013; Governato et al. 2012; Pontzen & Governato 2012; Brooks et al. 2013; Garrison-Kimmel et al. 2013).

stochastically from galaxy to galaxy, here we treat it as a free parameter with typical values  $\lambda \sim 0.05$  (e.g., Dutton et al. 2011; Kravtsov 2013).<sup>7</sup> Disk radii of the dwarf spheroidal progenitor objects at the point of the tidal truncation of mass assembly are shown in Figure 4. They increase with the halo mass much more steeply,  $R_{\text{disk}} \propto (M_{\text{TT},\epsilon})^{2/3}$  to  $R_{\text{disk}} \propto M_{\text{TT},\epsilon}$ , than a family of halos collapsing at the same redshift, which would have  $R_{\text{disk}} \propto M_{\text{halo}}^{1/3}$ .

We allow that a fraction  $f_{\text{disk}} \sim 0.5$  of the baryonic content of the halo resides in the disk; thus  $\int_0^{\infty} \Sigma(R) 2\pi R dR = f_{\text{disk}} f_b M$ . From this we find that the central surface mass density of the baryonic disk in the dwarf spheroidal progenitor objects is

$$\Sigma_0 = f_{\text{disk}} f_b \frac{M_{\text{halo}}}{2\pi R_{\text{disk}}^2}. \quad (21)$$

The resulting disk central surface densities are shown in Figure 4. In the S08 common mass scale family with  $M_{300} = 10^7 M_{\odot}$ , surface densities are in the range  $\Sigma_0 \sim (10 - 100) M_{\odot} \text{pc}^{-2}$ , sufficient for low-level star formation to proceed and yet insufficient, given the low metallicities, for a substantial gas fraction to transition into molecular form. The central surface density is particularly sensitive to the halo central density parametrized with  $M_{300}$ , a consequence of the sensitivity of the baryon fraction to the halo central density (see Section 3.2). In the common mass scale families with  $M_{300} \lesssim 0.5 \times 10^7 M_{\odot}$ , the surface densities are so low that these objects are utterly unable to form stars. On the other hand, the objects with  $M_{300} \gtrsim 2 \times 10^7 M_{\odot}$  seem to have surface densities sufficient to form dense molecular clouds even at relatively low metallicities.

### 4.2.2 Vertical Structure

The relative degree of rotational and pressure support can be estimated by evaluating the dimensionless ratio  $h/R$  of the vertical pressure scaleheight of the disk to the radius. When  $h/R \ll 1$ , the disk is geometrically thin and radial force balance is provided by rotation. When, at least formally,  $h/R \gtrsim 1$ , the equilibrium is not a true disk but a geometrically thick atmosphere in which radial force balance is provided by the hydrostatic pressure. The pressure scale can be estimated as the ratio of the effective (thermal and turbulent added in quadrature) velocity dispersion of the disk to the natural frequency of vertical oscillations,

$$h \sim \frac{c_{\text{eff}}}{\mu}. \quad (22)$$

The square of the frequency is given by the second derivative of gravitational potential along the vertical direction,

$$\mu^2 = \left. \frac{\partial^2 \Phi}{\partial z^2} \right|_{z=0}. \quad (23)$$

Both the halo and the disk contribute to the gravitational potential. The halo contribution and the corresponding vertical frequency  $\mu_{\text{halo}}$  can be straightforwardly computed from the NFW profile. The gravitational potential near the surface of a razor-thin disk is  $\Phi_{\text{disk}} = 2\pi G\Sigma|z|$ . Allowing for non-zero half-thickness  $h$ , we have  $\mu_{\text{disk}}^2 = (\partial^2 \Phi_{\text{disk}}/\partial z^2)|_{z \leq h} \sim 2\pi G\Sigma/h$ . Here,  $h$  implicitly depends on both the halo and the disk component. Solving for,

<sup>7</sup> The value that Dutton et al. (2011) quote,  $\lambda = 0.035$ , is defined relative to the virial radius  $r_{\text{vir}}$  which is somewhat larger than  $r_{200}$ . Kravtsov (2013) derives  $R_{\text{disk}} \approx 0.03 r_{200}$  corresponding to  $\lambda \approx 0.04$ .

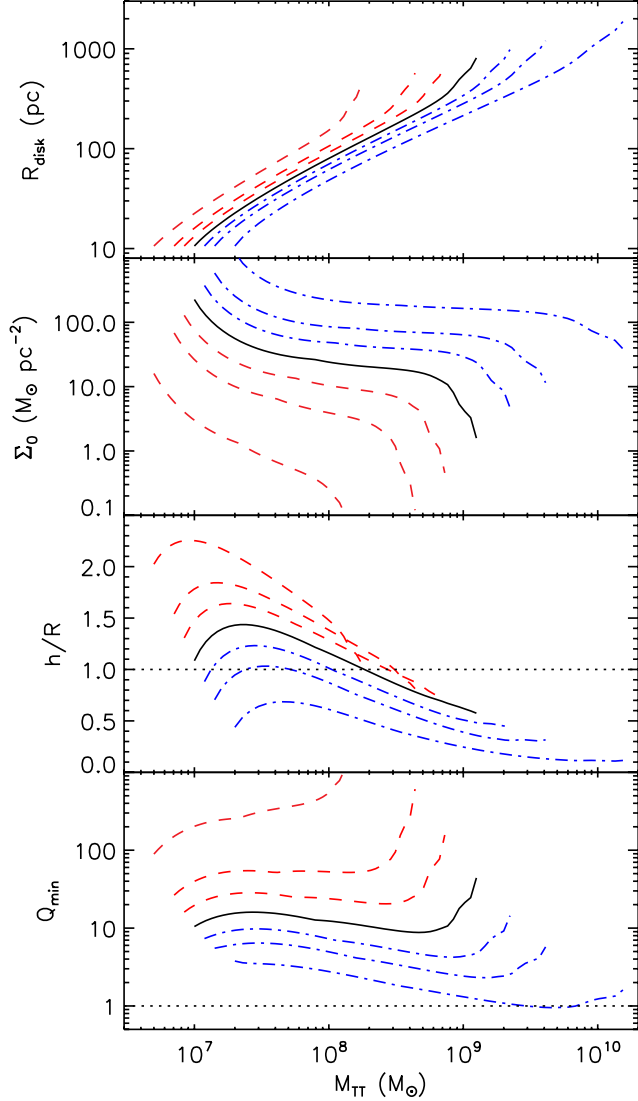


**Figure 4.** Properties of the baryonic content of dark matter halo of mass  $M_{\text{TT},0}$  belonging on the common mass scale relation  $M_{300} = 10^7 M_{\odot}$  at the point at which the external tidal field freezes the evolution of the inner density profile (solid lines). The panels from top to bottom show the radius of the gas disk  $R_{\text{disk}}$ , the central density of the gas disk  $\Sigma_0$ , the relative vertical disk scaleheight  $h/R$  evaluated at  $r = R_{\text{disk}}$ , and the minimum instability parameter of the disk  $Q_{\text{min}}$ . In computing these quantities, we assumed a spin parameter of  $\lambda = 0.05$  and a gas mass fraction in the disk of  $f_{\text{disk}} = 0.5$ . The dashed and dot-dashed lines show the neighboring common mass scale relations for  $M_{300} = (2^{-1}, 2^{-0.5}, 2^{-0.25})$  and  $(2^{0.25}, 2^{0.5}, 2^1) \times 10^7 M_{\odot}$ , respectively.

$\mu = (\mu_{\text{halo}}^2 + \mu_{\text{disk}}^2)^{1/2}$  we obtain

$$\mu = \frac{\pi G \Sigma}{c_{\text{eff}}} + \sqrt{\left(\frac{\pi G \Sigma}{c_{\text{eff}}}\right)^2 + \mu_{\text{halo}}^2}. \quad (24)$$

For simplicity we assume that  $c_{\text{eff}}$  is independent of  $z$ ; this is most certainly not the case as the low-dispersion CNM will reside closer to the midplane. In dwarf irregular galaxies,  $c_{\text{eff}}$  varies from  $\sim 15 \text{ km s}^{-1}$  in the warm phase HI to  $\sim 5 \text{ km s}^{-1}$  in the cold phase (e.g., Ianjamasimanana et al. 2012; Zhang et al. 2012, see also Stilp et al. 2013 as well as the theoretical results in Saury et al. 2013). The dwarf spheroidal progenitor disks with suppressed baryon frac-

tions seem to have  $\mu_{\text{halo}} \gtrsim \mu_{\text{disk}}$  for  $\lambda \sim 0.05$ , indicating that dark matter dominates vertical gravity.

In Figure 4, we plot  $h/R$  evaluated at  $R = R_{\text{disk}}$  for halos in the S08 common mass scale family and several neighboring families. We find that the disks with  $M_{\text{TT},0} \lesssim 10^8 M_{\odot}$  are typically thick with  $h/R \gtrsim 1$  for  $R \lesssim R_{\text{disk}}$ . Since, approximately,  $h/R \propto R^{-1/2}$ , the disks become thin at larger radii. Thus the inner radii of the gas disks can be pressure supported, especially towards lower halo masses. This resonates with the observation that the dwarf irregular galaxies seem to have solid-body like,  $V_{\text{HI}}(R) \propto R$  rotation curves in the centers. Such rotation curves are often interpreted as evidence for constant-density cores in the dark matter distribution, but could also arise simply due to pressure support at the innermost radii.

#### 4.2.3 Global Gravitational Stability

Gas disks that are globally gravitationally unstable develop bar mode perturbations which can rapidly transport angular momentum and deliver large gas masses to the gravitational centers. This drives rapid transformation of galaxy morphology, and as a result a compact massive stellar system, a nuclear star cluster or a stellar bulge, develops in the center. Pawlik et al. (2011, 2013) found this process to be particularly efficient in protogalactic disks assembling in  $\sim (10^8 - 10^9) M_{\odot}$  halos, assuming no reionization by external sources. Objects forming in the reionized universe and having reduced baryon fractions, however, may avoid this fate. Indeed, only some of the most luminous dwarf spheroidals in the Local Group, the Sagittarius Dwarf and NGC 205, contain stellar nuclei; the others seem to be described by single-component surface brightness profiles. We proceed to assess the potential for bar mode instability in the dwarf spheroidal progenitor objects.

For analytical simplicity of the forthcoming analysis, we assume that  $\lambda/\sqrt{2} \ll c^{-1}$  so that  $R_{\text{disk}} \ll r_s$ . The dark matter mass enclosed within radius  $r \lesssim R_{\text{disk}}$  is  $M_{\text{NFW}}(r) \approx (400\pi/3)\rho_{\text{crit}}c^3r^2r_s/\mathcal{M}(c)$ , where  $\rho_{\text{crit}}$  is the critical density of the universe and  $\mathcal{M}(x) = \ln(1+x) - x/(1+x)$ . The radial component of the gravitational force in the disk is baryon dominated at radii where  $\beta \int_0^r 2\pi\Sigma(R)RdR > M_{\text{NFW}}(r)$ , where  $\beta \approx \sqrt{r/R_{\text{disk}}} \lesssim 1$  is a reduction in the radial gravitational potential of the disk due to its flattened nature.<sup>8</sup> This condition is most likely to be satisfied at  $r \approx 0.8 R_{\text{disk}}$ . At this reference radius, the condition becomes

$$\lambda < \sqrt{\frac{0.5 f_{\text{disk}} f_b \mathcal{M}(c)}{c^2}} \quad (\text{baryon domination}). \quad (25)$$

For reference values  $f_{\text{disk}} = 0.5$ ,  $c = 4$ , and a baryon fraction substantially reduced from the cosmic mean  $f_b = 0.1 \Omega_b/\Omega_m$  (see Section 3.2), baryon domination requires an improbably small disk spin parameter,  $\lambda \lesssim 0.01$ . For the typical disk spin parameter  $\lambda \sim 0.05$ , dark matter gravity dominates the radial gravitational force throughout unless the baryon fraction is close to the cosmic mean.

In disks that are not geometrically thin, a refinement of the criterion in Equation (25) may be required. If the rotationally supported disk is thin and the radial pressure gradient can be neglected, the disk is stable to bar mode excitation if the baryons dominate the radial component of the gravitational force (e.g., Christodoulou

<sup>8</sup> The square root is a fitting function approximating the value of  $\beta$  in the specific case of a razor-thin exponential disk embedded in a  $\rho \propto r^{-1}$  halo.

et al. 1995, their Section 3.4.4). If the gas pressure gradient contributes significantly to the radial force balance, this reduces the threshold for stability. Fridman & Poliachenko (1984), in their Part V, Section 4.5.2, find that in a toy model of a uniformly rotating disk embedded in a halo, the disk-to-halo mass ratio  $M_{\text{disk}}/M_{\text{halo}}$  at which the instability sets in increases with the factor  $(1-\Pi)/(1-2\Pi)$ , where  $\Pi$  denotes the fractional reduction of the gravitational force by the pressure force. In this simplified model, pressure stabilizes the bar mode for  $\Pi \geq 1/2$ . With the vertical structure derived in Section 4.2.2, the pressure averaged over one scale height of the disk is  $P \sim \Sigma c_{\text{eff}}^2/(2h)$  and the pressure gradient acceleration is  $a_P \sim c_{\text{eff}}^2/R_{\text{disk}}$ . For disks on the verge of global instability, we can compare *twice* the gravitational acceleration due to the halo,  $a_{\text{grav}} \sim 2GM_{\text{NFW}}(r)/r^2$ , to the pressure gradient acceleration, to find  $\Pi \sim a_P/a_{\text{grav}} \sim 1.4(c_{\text{eff}}/V_{200})^2/\lambda_{0.05}$ , where in the last step we substituted  $c = 4$  and  $\lambda_{0.05} = \lambda/0.05$ . This confirms that in low-mass halos with low  $V_{200}$ , the global (bar mode) instability can be partially stabilized by the radial pressure force.<sup>9</sup>

#### 4.2.4 Local Gravitational Stability

Local stability of the HI disk requires  $Q = \kappa c_{\text{eff}}/(\pi G \Sigma) > 1$ , where  $\kappa$  is the epicyclic frequency. In a disk of a finite thickness, and considering short wavelength radial perturbations with wave numbers  $k$ , the effective gravity is reduced by the factor  $\sim (1 + kh)^{-1}$ , implying local stability for  $Q > Q_{\text{crit}} \sim 0.5 - 1$ . For rotational profiles due to the dark matter halo only,  $\kappa \sim \sqrt{3GM_{\text{NFW}}(R)/R^3} \sim \sqrt{3}\Omega \propto R^{-1/2}$ . Thus, if  $c_{\text{eff}}$  is approximately independent of radius and  $R_{\text{disk}} \ll r_s$ , the disk is the most susceptible to local instability at  $R \sim R_{\text{disk}}/2$ ; for  $R_{\text{disk}} \sim r_s$ , the radius of highest susceptibility shifts to  $R \sim R_{\text{disk}}$ . In Figure 4, we plot  $Q$  evaluated at  $R = R_{\text{disk}}/2$  in the dwarf spheroidal progenitor disks. We find that  $Q_{\text{min}} \gg Q_{\text{crit}}$  at all parameter values. This shows that due to the sharply suppressed baryon fractions, HI disks in the common mass scale progenitor objects are stable to the local gravitational instability of the disk. The disks become marginally unstable only when the common mass scale parameter is at least twice the S08 value,  $M_{300} \gtrsim 2 \times 10^7 M_{\odot}$ . Very speculatively, the local gravitational instability of the HI disk, which starts setting in halos experiencing tidal truncation of their mass assembly at masses  $\sim 5 \times 10^9 M_{\odot}$ , may be associated with the development of conditions for massive stellar cluster formation in the disk. Some of them may be the progenitors of the metal poor globular clusters as in the scenario of Kravtsov & Gnedin (2005). The massive clusters can also migrate into the galaxy center and build a nuclear star cluster (e.g., Agarwal & Milosavljević 2011).

#### 4.2.5 Disk Edges

The HI disk extends to the maximum radius at which the gas surface density is sufficient for a neutral layer to be present that is shielding itself from the intergalactic ionizing background. Letting  $f = 10^5 f_5 \text{ cm}^{-2} \text{ s}^{-1}$  denote the ionizing photon number per unit area per unit time and assuming that the disk midplane remains neutral and opaque to ionizing photons, the number of photons absorbed per unit area of the disk per unit time is  $\sim f/4$ . The maximum disk surface density that can be in the ionized

state on each face of the disk is given by the Strömgen condition  $\alpha_{\text{rec}}[\frac{1}{2}\Sigma_{\text{HII}}X/(h_{\text{HII}}m_p)]^2 \sim \frac{1}{4}f/h_{\text{HII}}$ . Here,  $X \sim 0.75$  is the hydrogen mass fraction and  $\alpha_{\text{rec}}$  is the recombination coefficient, which we take to be the average of the case A and B coefficients  $\alpha_{\text{rec}} \sim 3 \times 10^{-13} \text{ cm}^3 \text{ s}^{-1}$ . Denoting the effective sound speed in the ionized gas with  $c_{\text{HII}} = 10^6 c_{\text{HII},6} \text{ km s}^{-1}$  and the vertical scale height of the ionized gas layer with  $h_{\text{HII}} \sim c_{\text{HII}}/\mu_{\text{halo}}$ , we find that the critical surface density for the presence of a neutral layer is  $\Sigma_{\text{HII,crit}} \sim (0.1 - 0.2) f_5^{1/2} c_{\text{HII},6}^{1/2} M_{\odot} \text{ pc}^{-2}$ , with the numerical coefficient increasing with  $M_{\text{TT},\epsilon}$ . This estimate assumes that the radius of the edge is much smaller than the halo scale radius  $r_s$ . Relaxing this assumption would result in a lower  $\mu_{\text{halo}}$  and higher  $\Sigma_{\text{HII,crit}}$ . The critical surface density at which HI disk edges in more massive systems are found in the local universe,  $\sim 0.4 M_{\odot} \text{ pc}^{-2}$ , lies slightly above this range. The ionizing background first increases to  $z \sim 2$  and then decreases toward even high redshifts (e.g., Faucher-Giguère et al. 2009; Haardt & Madau 2012).<sup>10</sup> This could raise the critical disk edge surface density up to a maximum of  $\sim 1 M_{\odot} \text{ pc}^{-2}$ . Comparing these thresholds to the surface densities in our model, we can conclude that HI disk edges in dwarf spheroidal progenitor objects will occur at  $\sim (2 - 3) R_{\text{disk}}$ . We also conclude that the disks in  $M_{300} \lesssim 5 \times 10^6 M_{\odot}$  halos with substantially reduced baryon fractions will not contain any neutral gas over their entire history.

#### 4.2.6 Dependence on Angular Momentum

The results of this section are potentially sensitive to the angular momentum of the gas that has settled in the protogalactic disk. For disk angular momenta exceeding the fiducial value  $\lambda = 0.05$  assumed here, we expect the qualitative conclusions to remain unchanged, with a higher fraction of disk gas having surface densities below the threshold for the WNM-to-CNM transition. For atypically small angular momenta,  $\lambda \ll 0.05$ , however, the central column density could become high enough to allow the atomic-to-molecular transition in the inner part of the disk, potentially triggering intense central star formation, and potentially even explosive baryon removal by SNe (see Section 4.4 below). The randomness inherent in hierarchical merging guarantees that  $\lambda$  samples the full range of values, occasionally dipping well below our fiducial choice, especially in certain major mergers between halos. While disk buildup from cold-mode accretion in more massive halos produces characteristically high values of spin parameter  $\lambda \sim 0.1$  (Stewart et al. 2013), dedicated cosmological simulations are required to assess the angular momentum content of the baryons in small, reionized halos

### 4.3 From Tidal Truncation to Ram Pressure Stripping

Mayer et al. (2006) have determined that dwarf spheroidal satellites with maximum circular velocities  $V_{\text{max}} < 30 \text{ km s}^{-1}$  are completely ram pressure stripped if their orbits have pericenters of  $\lesssim 50 \text{ kpc}$  from the center of the Milky Way. Generally, as we have remarked in Section 2.1, the redshift at which the gas is ram pressure stripped will be somewhat lower than that of the tidal

<sup>9</sup> Consistent with this analysis, dwarf irregular galaxies, seen here as dwarf spheroidal satellites' analogs in the field, exhibit increasing relative disk thickness with decreasing luminosity (Roychowdhury et al. 2013).

<sup>10</sup> Schaye (2004) argues for a high effective value  $f_5 \sim 10$  of the ionizing photon flux in the local galaxies, but this seems high and possibly in tension with the upper limit of Adams et al. (2011).

truncation of the halo’s mass assembly  $z_{\text{TT}}(M_{\text{TT}})$ . In the interval  $z_{\text{ram}} < z < z_{\text{TT}}$ , the neutral gas in the halo may temporarily remain, allowing some final star formation to proceed. If tidal truncation takes place when the common mass scale object has approached to within  $r \sim 3 r_{200,\text{MW}}$  of a Milky Way progenitor halo of radius  $r_{200,\text{MW}}$ , and the ram pressure stripping happens when the object has approached to within  $r \sim r_{200,\text{MW}}$  (formally, the point of incorporation into the Milky Way’s or Andromeda’s satellite population), then we can estimate the time an object infalling radially from rest at a large distance traverses this radial range. We assume that the outer NFW profile approximates the spherically averaged mass distribution to multiple virial radii (see, e.g., Masaki et al. 2012). The time interval has a negligible dependence on the halo concentration and approximately equals

$$\Delta t_{\text{TT} \rightarrow \text{ram}} \sim 0.13 H(z)^{-1}, \quad (26)$$

where  $H(z)$  is the Hubble parameter at redshift  $z$ . This time is of the same order of magnitude as the growth time of the infalling halo prior to tidal truncation. Thus, if other processes, such as ram pressure stripping by large-scale structure flows and galactic outflows, do not remove the star forming gas before the infall, star formation in the period between tidal and ram pressure stripping should be taken into account when estimating the final stellar mass of the object.

#### 4.4 Simmering Star Formation and the Unlikelihood of Outflows

The local gravitational stability of the HI disk does not imply the absence of star formation, because the WNM, if overpressured by turbulence, can become thermally unstable and cool by metallic fine structure line emission to form transient concentrations of cold neutral gas. In pressure equilibrium, the low-filling-factor CNM is  $\sim 100$  times denser than the WNM in which it is entrained and has a Jeans length shorter by the same factor (e.g., Vázquez-Semadeni 2009, 2012; Saury et al. 2013). Stars can form when turbulence collects a sufficient mass of CNM to cross the threshold for gravitational instability in the CNM alone. The typical Jeans masses are of the order of  $M_{\text{J}} \sim 10^3 M_{\odot}$ , which is marginally sufficient for the collapsing gas clump, upon turbulent gravitational fragmentation, to form stars sampling the entire stellar initial mass function (IMF). However, because of the stochasticity of the local CNM buildup, larger star forming complexes are unlikely to form, consistent with the observation that dwarf galaxies in the local universe (typically more massive than the common mass scale progenitor systems) seem to form only a small fraction of their stars in the starburst mode (Lee et al. 2009). Given this, we expect that the star formation proceeded very slowly in typical dwarf spheroidal progenitor disks, with at most a few isolated  $\sim M_{\text{J}}$  sites, each containing a handful of massive young stars, being present at any time. The feedback from such low-grade, distributed star formation in the form of H II regions and SNe seems insufficient to drive explosive removal of baryons from the halos. At best, it can remove gas from the disk and deposit it in the enveloping diffuse gaseous halo, from where it can condense back into the disk, enriching it with the nucleosynthetic return of preceding stellar generations, now diluted through turbulent mixing in the halo (see Section 5.2 below). Therefore, *we ignore the feedback and assume that the dwarf spheroidal progenitor objects do not lose their baryons to outflows*, in contrast with the outflows detected in, say, the substantially more massive Ly $\alpha$  emitting and Lyman break galaxies.

The assumption of negligible feedback may seem to contradict some analyses suggesting that SNe efficiently drive baryons from atomically cooling halos, as it may be naively expected on purely energetic grounds. A closer consideration, however, reveals that clumpiness of the protogalactic gas diminishes the destructive impact of the SNe, in particular if they explode with energies similar to those of the typical core-collapse SNe in the nearby universe, rather than the ultra-energetic and much more destructive pair-instability SNe (see, e.g., Greif et al. 2007; Wise & Abel 2008). For example, Wise et al. (2012) carried out a high resolution cosmological simulation tracking star formation, reionization, SNe, and chemical enrichment in halos during the epoch of reionization. Their representative “quiet” halo attaining a final mass of  $\sim 10^8 M_{\odot}$  at  $z = 7$  still manages to retain a baryon fraction  $f_{\text{b}} \sim 0.5 \Omega_{\text{b}}/\Omega_{\text{m}}$ , in spite of having converted  $\gtrsim 10^5 M_{\odot}$  of its baryons into stars; their “intense”  $\sim 10^9 M_{\odot}$  halo retains close to all of its baryons while forming an  $\sim 2 \times 10^6 M_{\odot}$  star cluster. The dwarf spheroidal progenitor halos we envision have reduced baryon fractions at the outset. Therefore, we expect that their star formation would have proceeded even more quietly and, thus, that the impact of SNe on the baryon budget would have been even weaker.

Dwarf irregular galaxies residing in more massive dark matter halos than those of the Milky Way’s dwarf spheroidal satellites do exhibit starbursts and coherent galactic outflow signatures (Martin 1998, 1999). These outflows can be interpreted as having been triggered by periodic destabilization and central channeling of gas in mergers. We expect that in these more massive dwarf galaxies with higher  $V_{\text{max}}$ , baryon fractions are closer to the cosmic mean and the gas disks are closer to the threshold for global gravitational instability that, if triggered by a merger event, can produce a concentrated starburst.

## 5 RESULTS

### 5.1 Stellar Masses and Half-Light Radii

Assuming that neutral gas turns into stars on the time-scale  $\tau_{\text{dep}}$  given by Equation (18), the star formation rate is

$$\dot{M}_{\star} = \frac{M_{\text{HI}}}{\tau_{\text{dep}}}, \quad (27)$$

where  $M_{\text{HI}}$  is the HI mass in the most massive progenitor branch of a halo’s merger tree. We ignore any star formation that may have occurred in the minor branches of the merger tree representing smaller halos merging with the main branch. This approximation is justified by the strong dependence in Equation (16) of the baryon fraction at any given redshift on the mass of a low-mass halo. The minor halos will on average have severely suppressed baryon fractions and will be unable to sustain self-shielding HI disks and form stars of their own. We also approximately neglect the actual depletion of the neutral gas to star formation. Given the long depletion time, this is clearly a good approximation for objects ending star formation at  $z \gg 1$ , but even at lower redshifts, the depletion of the HI disk is compensated in part by the stellar mass return and recombination from the fraction  $(1 - f_{\text{disk}})$  of the baryonic content that remains outside the disk. Therefore

$$M_{\text{HI}} \approx f_{\text{disk}} f_{\text{b}} M_{\text{halo}}, \quad (28)$$

and with this, the zero-age main sequence (ZAMS) stellar mass of a dwarf spheroidal is

$$M_{\star} = M_{\star,\text{TT}} + M_{\star,\text{TT} \rightarrow \text{ram}}, \quad (29)$$

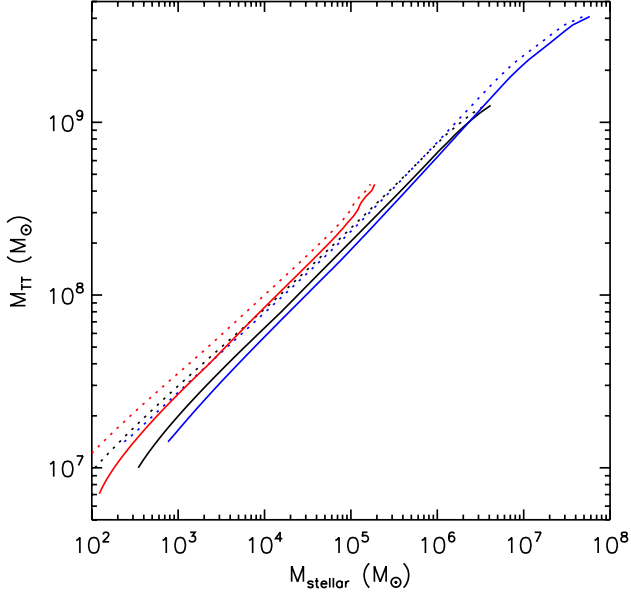


**Figure 5.** The halo mass at the point at which an external tidal field truncated the mass assembly of the dwarf spheroidal progenitor halo as a function of the stellar mass for halos on the common mass scale relation with  $M_{300} = (2^{-0.5}, 2^0, 2^{+0.5}) \times 10^7 M_\odot$  (red, black, and blue lines, respectively), excluding and including star formation in the period between tidal and ram pressure stripping (dotted and solid lines, respectively).

where

$$M_{\star, \text{TT}} \approx \frac{f_{\text{disk}}}{\tau_{\text{dep}}} \int_{z_{\text{TT}}}^{\infty} f_{\text{b}}(M_{\text{MMP}}[M_{\text{TT}}, z_{\text{TT}}; z], z) \times M_{\text{MMP}}[M_{\text{TT}}, z_{\text{TT}}; z] \frac{dt}{dz} dz \quad (30)$$

is the stellar mass produced until the point of the tidal truncation of the object's mass assembly,  $dt/dz = (1+z)^{-1}H(z)^{-1}$ , and

$$M_{\star, \text{TT} \rightarrow \text{ram}} \approx \frac{f_{\text{disk}}}{\tau_{\text{dep}}} f_{\text{b}}(M_{\text{TT}}, z_{\text{TT}}) M_{\text{TT}} \Delta t_{\text{TT} \rightarrow \text{ram}} \quad (31)$$

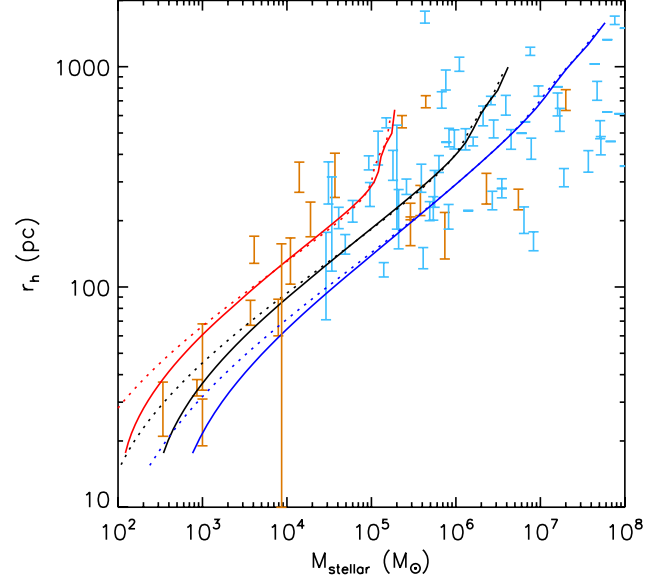
is the star formation taking place after tidal truncation but before the halo's gas has been ram pressure stripped.

Figure 5 shows the dependence of  $M_{\text{TT}, \epsilon}$  on  $M_\star$  for three representative common mass scale families,  $\epsilon = (-0.15, 0, +0.15)$ , we assume that a factor of  $f_{\text{ZAMS}} = 0.5$  of the ZAMS stellar mass remains at  $z = 0$  after stellar mass loss. The  $M_{\text{TT}, \epsilon}(M_\star)$  is largely independent of the central density parameter  $\epsilon$ . A variation of  $\approx 2$  dex in halo mass corresponds to a much larger variation of  $\approx 4$  dex in stellar mass, so that, approximately

$$M_\star \propto M_{\text{TT}}^2. \quad (32)$$

This can be understood as arising from the scaling of the stellar mass with *both the mass of the host halo, and the duration of the time available for star formation*, where the latter is itself a roughly linearly increasing function of the halo mass. Including the parametric dependence on the halo mass fraction in the disk  $f_{\text{disk}}$  and the gas-to-star conversion time-scale  $\tau_{\text{dep}}$ , we have

$$M_\star \approx 2 \times 10^4 M_\odot \left( \frac{f_{\text{disk}}}{0.5} \right) \left( \frac{f_{\text{ZAMS}}}{0.5} \right) \times \left( \frac{\tau_{\text{dep}}}{10 \text{ Gyr}} \right)^{-1} \left( \frac{M_{\text{TT}}}{10^8 M_\odot} \right)^2, \quad (33)$$



**Figure 6.** The half-light radius as a function of the stellar mass for halos on the common mass scale relation with  $M_{300} = (2^{-0.5}, 2^0, 2^{+0.5}) \times 10^7 M_\odot$  (red, black, and blue lines, respectively), excluding and including star formation in the period between tidal and ram pressure stripping (dotted and solid lines, respectively). The data points denote dwarf spheroidal satellites of the Milky Way (brown) and Andromeda (light blue) from McConnachie (2012). The half-light radius uncertainties were arbitrarily assigned to zero where McConnachie does not quote uncertainties. The stellar masses assume solar mass-to-light ratios  $M_\star/L = M_\odot/L_\odot$ ; the actual mass-to-light ratios could be up to a factor of  $\sim 2$  higher.

again approximately independent of the central density quantified by  $M_{300}$ .<sup>11</sup>

Figure 6 plots our calculated dwarf spheroidal half-light radii as a function of the present-day stellar mass. The figure shows the half-light radii and stellar masses of the dwarf spheroidal satellites of the Milky Way and Andromeda in the compilation of McConnachie (2012). We assume that the half-light radius is related to the exponential scalelength of the disk via  $r_h = 1.7 R_{\text{disk}}$  where  $R_{\text{disk}} = 0.05 r_{200}/\sqrt{2}$ , and arrive at the final value of half-light radius by computing the stellar mass-weighted average of  $r_h$  over each most massive progenitor track. We also assume that the stellar mass-to-light ratio has the solar value,  $M_\star/L = M_\odot/L_\odot$ . The latter two assumptions are almost certainly not very accurate. The stellar IMF will likely evolve (see Geha et al. 2013) as the metallicities of the gas disks increase with time and the CMB temperature floor drops. In our crude model, the dependence on the IMF is encapsulated in the parameter  $f_{\text{ZAMS}}$ , with more top-heavy IMFs

<sup>11</sup> The stellar mass-halo mass relations in Equations (32) and (32) are significantly shallower than the ad hoc relations ranging in slope from  $M_\star \propto M_{\text{TT}}^{2.5}$  to  $M_\star \propto M_{\text{TT}}^3$  adopted elsewhere (Koposov et al. 2009; Kravtsov 2010; Ocvirk & Aubert 2011; Rashkov et al. 2012) to explain the properties of the dwarf population. The ostensible success of the steep scaling in reproducing the dwarf luminosity function is consistent with the conclusions of Brook et al. (2013) that straightforward halo mass-stellar mass abundance matching mandates a steep scaling  $M_\star \propto M_{\text{TT}}^{3.1}$ . However the difficulty with reproducing the observed halo densities and maximum circular velocities (Boylan-Kolchin et al. 2011, 2012) suggests that the assumptions of completeness and monotonicity entering the straightforward abundance matching may be questionable.

implying lower  $f_{\text{ZAMS}}$  and  $M_*$ . Theoretical work is in progress to develop a theory of the stellar IMF at low column densities and metallicities and high redshifts (Safranek-Shrader et al. 2014).

The stellar masses and half-light radii provided by the model, especially allowing for a relatively small, 0.15 – 0.3 dex variation of the common mass scale parameter  $M_{300}$  around the S08 value, seem to be in close agreement with those of the observed dwarf spheroidal satellites. This reproduces the observed  $\approx 5$  dex variation of the stellar mass across the dwarf spheroidal satellite sequence in the Milky Way. The ultra-faint dwarfs reside in dark matter halos that were near, or slightly above, the atomic cooling threshold,

$$M_{\text{halo, UFD}} \lesssim 2 \times 10^8 M_{\odot}, \quad (34)$$

when they formed the bulk of their stars.

## 5.2 Chemical Evolution

We argued in Section 4.4 above that star formation in the dwarf spheroidal progenitor objects takes place in the simmering rather than the starburst mode, and that such slow star formation is not likely to drive outflows powerful enough to remove the star formation’s nucleosynthetic return from the halo. This hypothesis has immediate implications for the objects’ chemical evolution. To explore these implications, we estimate the dependence of the metallicity on the stellar mass. Let  $f_{\text{ret}}$  denote the fraction of the stellar mass returned by winds and SNe, and let  $Z_{\text{ret}}$  be the metallicity of the returned mass. Assuming a negligible contribution from an initial (Pop III) pre-enrichment that would have not left behind surviving low-mass stars, as well as instantaneous return (i.e., through core-collapse ejecta and other potential prompt mechanisms) and instantaneous and homogeneous mixing in the entire gas mass of the halo, we have that the metallicity of the gas in the halo is given by

$$Z_{\text{gas}} \sim Z_{\text{ret}} \frac{f_{\text{ret}} M_*}{f_b M_{\text{halo}}}, \quad (35)$$

where  $M_*$  and  $f_b$  are the stellar mass and the baryon fraction in the halo of mass  $M_{\text{halo}}$ . It is important to note that Equation (35) allows for baryons to be added by minor branches of the merger tree and by accretion from the IGM, but it assumes that the added baryons are in the form of a chemically pristine gas and that this gas mixes instantaneously with the metal-enriched gas residing in the main branch.

The average stellar metallicity will then be given by

$$Z_{*, \text{TT}} \sim \frac{1}{M_{*, \text{TT}}} \int_{z_{\text{TT}}}^{\infty} Z_{\text{gas, MMP}}(z') \times \dot{M}_{*, \text{MMP}}(z') \frac{dt}{dz'} dz'. \quad (36)$$

Substituting Equations (27) and (28) we obtain

$$Z_{*, \text{TT}} \sim f_{\text{disk}} f_{\text{ret}} Z_{\text{ret}} \frac{\tau_{\text{rep, TT}}}{\tau_{\text{dep}}}, \quad (37)$$

where

$$\tau_{\text{rep, TT}} = \frac{1}{M_{*, \text{TT}}} \int_{z_{\text{TT}}}^{\infty} M_{*, \text{MMP}}(z') \frac{dt}{dz'} dz' \quad (38)$$

is a “reprocessing time,” a measure of the time-scale on which the object has become enriched with metals. The reprocessing in the period from the onset of tidal truncation to the final ram-pressure

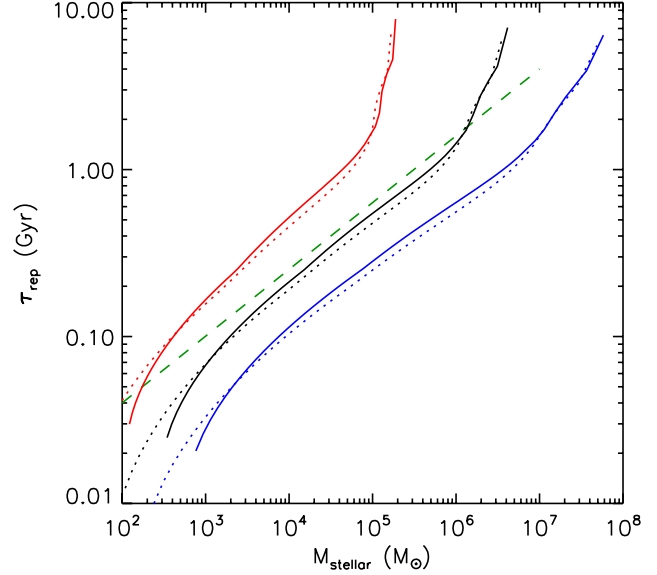


**Figure 7.** The self-enrichment time-scale  $\tau_{\text{rep}}$  as a function of the stellar mass for halos on the common mass scale relations with  $M_{300} = (2^{-0.5}, 2^0, 2^{+0.5}) \times 10^7 M_{\odot}$  (red, black, and blue lines, respectively), excluding and including star formation in the period between tidal and ram pressure stripping (dotted and solid lines, respectively). The green dashed line of arbitrary normalization indicates the slope of the  $M_* - \tau_{\text{rep}}$  relation required for Equation (37) to reproduce the iron abundance-stellar mass correlation  $Z_{\text{Fe}} \propto M_*^{0.4}$  in the Milky Way dwarf spheroidals of Kirby et al. (2011a) under the artificial assumption that the iron synthesis rate is proportional to the instantaneous star formation rate.

stripping of the gas can be included by modifying Equation (37) to read

$$Z_* \sim f_{\text{disk}} f_{\text{ret}} Z_{\text{ret}} \frac{\tau_{\text{rep}}}{\tau_{\text{dep}}}, \quad (39)$$

where

$$\tau_{\text{rep}} = \frac{1}{M_*} \left[ (\tau_{\text{rep, TT}} + \Delta t_{\text{TT} \rightarrow \text{ram}}) \dot{M}_{*, \text{TT}} + \frac{1}{2} (\Delta t_{\text{TT} \rightarrow \text{ram}})^2 \dot{M}_*(z_{\text{TT}}) \right]. \quad (40)$$

The metallicity  $Z_*$  in Equation (39) is proportional to a product of several uncertain factors and cannot be predicted robustly. Therefore, we refrain from directly plotting  $Z_*$ . Instead, in Figure 7 we plot the arguably more robust reprocessing times  $\tau_{\text{rep, TT}}$  and  $\tau_{\text{rep}}$  as functions of the stellar mass for three neighboring common mass scale families. The times vary from mere tens of Myr at the low-mass end to almost 10 Gyr at the high-mass end. The reprocessing times as a function of the stellar mass exhibit a sharp upturn when the time exceeds  $\sim 1$  Gyr, corresponding to halos with  $z_{\text{TT}} \lesssim 2$ . The upturn mass increases from  $10^5 M_{\odot}$  to  $10^7 M_{\odot}$  for  $M_{300}$  increasing from  $0.7 \times 10^7 M_{\odot}$  to  $1.4 \times 10^7 M_{\odot}$ .

For illustration, with the specific choices  $f_{\text{disk}} = f_{\text{ret}} = 0.5$  and  $Z_{\text{ret}} = 0.05$  (all of which are uncertain), we have

$$Z_* \approx \frac{\tau_{\text{rep}}}{\tau_{\text{dep}}} Z_{\odot}, \quad (41)$$

implying that the metallicities of the dwarf spheroidals resulting from the prompt, core-collapse-type enrichment should vary over two orders of magnitude, from  $\sim 10^{-2.3} Z_{\odot}$  (for  $M_{300} = 10^7 M_{\odot}$  and  $M_* \gtrsim 10^3 M_{\odot}$ ) to just below  $Z_{\odot}$ . This degree of metal-

licity variation seems similar to that found in the observed stellar mass-metallicity relation (Kirby et al. 2011a), where the dwarf iron abundance scales with the stellar mass as  $Z_{\text{Fe}} \propto M_{\star}^{0.4}$ . The stellar mass dependence of the reprocessing time in Figure 7 seems to agree with this slope (green dashed line in the figure) up to the point of upturn. If the average iron yield of core-collapse SNe is  $Z_{\text{ret,Fe}}/Z_{\text{ret}} \sim 0.1$  and the solar iron abundance is  $Z_{\odot,\text{Fe}}/Z_{\odot} \approx 0.2$ , then the model predicts an average iron abundance spanning the range  $-2.6 \lesssim \langle [\text{Fe}/\text{H}] \rangle < -0.3$ .

Allowing for SNe Ia to introduce an iron abundance enhancement of  $\Delta\langle [\text{Fe}/\text{H}] \rangle \sim +0.3$  at the high-mass end of the Milky dwarf spheroidal sequence, but not at the low-mass end (since these dwarfs are ram pressure stripped on time-scales relatively short compared to the typical SN Ia delay times), the range widens to match the observations (see Kirby et al. 2011a). The statistics of delay times  $\tau_{\text{a}}$  for the onset of SN Ia enrichment is currently poorly determined and thus it is not possible to carry out a systematic comparison with the reprocessing times  $\tau_{\text{rep}}$ . All dwarf spheroidals seem to exhibit signatures of SN Ia enrichment except for the ultra-faint dwarfs Segue 1 and Ursa Major II, which exhibit  $\alpha$ -enhancement in all the stars with medium-resolution spectroscopy-based abundance measurements, consistent with pure core-collapse nucleosynthesis (Vargas et al. 2013). If the delay time is, say,  $\tau_{\text{a}} \sim 0.1$  Gyr, then our model indeed allows for pure core-collapse enrichment only in the faintest dwarfs, consistent with the observations (see, also, Frebel & Bromm 2012, who reached a similar, slightly less restrictive conclusion based on the analysis of a smaller stellar sample).

We do not compute the metallicity distribution functions and are not in the position to compare the predictions of this model with the logarithmic and linear stellar metallicity scatter of the observed dwarfs. The assumption of instantaneous mixing implied in Equation (35) precludes a realistic computation of the scatter. A more accurate approach, which we defer to further study, would include a model in which chemical enrichment is stochastic and non-instantaneous (e.g., Oey 2000, 2003; Pan & Scalo 2007). Finally, we note that because of the metal dilution in the gas mass accumulating until the onset of tidal truncation, it seems unlikely that potential pre-enrichment by Pop III SNe would have significantly affected the mean metallicity of the galaxy, but it could have certainly left its imprints in the structure of the low-metallicity tail of the metallicity distribution.

## 6 WHERE ARE THE DENSEST SATELLITES?

Boylan-Kolchin et al. (2012) compared the densities of the Milky Way’s dwarf spheroidal satellites derived from stellar kinematical measurements to those of the most massive satellites of Milky Way-equivalent galaxies in a cosmological simulation, and found that the simulated halos contained satellites that were denser than the observed dwarfs. The simulated halos contained at least 10 subhalos with maximum circular velocities  $V_{\text{max}} > 25 \text{ km s}^{-1}$ , higher than allowed for objects lying on the common mass scale relation (see Section 2.1 and Figure 1). These objects have been called “too big to fail” (Boylan-Kolchin et al. 2011), because of having deeper gravitational potential wells than the observed common mass scale objects, which are consistent with  $V_{\text{max}} \sim (10 - 30) \text{ km s}^{-1}$  (Strigari et al. 2010); they should have retained even higher baryon fractions and formed more luminous, easily detectable stellar systems (e.g., Kravtsov et al. 2004).

There have been attempts to resolve the too-big-to-fail prob-

lem by considering the possibility that the dwarf spheroidal satellite population of the Milky Way is a statistical outlier or that it reflects an overestimate of the mass of the Milky Way’s dark matter halo. Purcell & Zentner (2012) find that a subsample of realizations of Milky Way-analog halos in CDM simulations have satellite densities consistent with the observations, and argue that the problem with densities can be explained on statistical grounds. Strigari & Wechsler (2012), however, find that the Milky Way is not a statistical outlier in its number of bright satellites as compared to similar galaxies in *Sloan Digital Sky Survey*. Others (e.g., Wang et al. 2012; Vera-Ciro et al. 2013) attempt to address the problem by invoking the possibility that the mass of the Milky Way halo is lower than normally assumed, which reduces the expected number of satellites with high maximum circular velocities.

We propose a different, very speculative solution to the too-big-to-fail problem, that a number of satellite subhalos with circular velocities above the range consistent with the common mass scale objects are indeed present in the Local Group, but that the stellar systems in these “too-big-to-fail” satellites are not being identified with the dwarf spheroidal morphological type, but with an altogether different type of stellar system. Recall that because the most massive progenitor accretion histories of halos with similar central densities are themselves similar (Section 2.2), the most massive progenitors of the subhalos with  $M_{300} \gg 10^7 M_{\odot}$  will have already had masses  $M_{\text{MMP}} \gtrsim 10^8 M_{\odot}$  at  $z = 10$ , and as such, they will have been able to form their first stellar generations before reionization and to retain baryon fractions  $\sim \Omega_{\text{b}}/\Omega_{\text{m}}$  after reionization. It is our general expectation that in gas-rich early halos retaining high baryon fractions, especially those with gas accretion times much shorter than the typical gas-to-stars conversion time at high surface densities  $\sim 1$  Gyr, global gravitational instabilities facilitate rapid angular momentum transport and drive large gas masses into the halo centers. This is clearly seen in the simulations of Pawlik et al. (2011, 2013) tracking the formation of a  $10^9 M_{\odot}$  halo at  $z = 10$  with no external ionizing sources, where the bar mode instability transported between a quarter and a third of the baryons in the halo into the inner few tens of parsecs.

The morphological type of the resulting stellar system will differ from that of a non-nucleated dwarf spheroidal galaxy. The system will at least contain a dense central stellar cluster. The star formation that produced the system will have been much more intense than in the extended, gravitationally stable disk in baryon-poor halos described in Section 4. This intense nuclear star formation might drive an explosive removal of baryons from the halo, possibly foiling star formation altogether outside the central cluster. The Local Group already contains dense, centrally concentrated stellar systems including the compact elliptical galaxy M32 and the massive globular clusters  $\omega$  Centauri of the Milky Way and Mayall II (or G1) of Andromeda. It also contains less dense, spheroidal stellar systems with embedded dense nuclear stellar components, such as the nucleus of the spheroidal galaxy NGC 205 and the nuclear globular cluster M54 of the Sagittarius dwarf spheroidal galaxy. There is currently no evidence for dark matter in  $\omega$  Cen and G1, but a dark matter halo with a density comparable to that of the densest dwarf spheroidal galaxies is consistent with the kinematic data (K. Gebhardt, priv. comm.).

Interestingly, the stellar metallicity spreads in  $\omega$  Cen and M54 are larger than those in typical globular clusters and are similar to the spreads in dwarf galaxies (e.g., Leaman 2012; Willman & Strader 2012); the same may be true for G1 (Meylan et al. 2001). The large spreads can be interpreted as indirect evidence that the stars in these clusters formed in the gravitationally confining cen-

tral density cusps of dark matter halos, rather than, say, in the fragmentation of locally gravitationally unstable extended galactic gas disks, or in the collision of gas streams in galaxy mergers, the latter two being the standard mechanisms thought to produce globular clusters.

It is often taken for granted that to reconcile a galaxy-like origin with the compact present form of stellar systems like  $\omega$  Cen, an outer, more extended, dwarf spheroidal-like, low-surface-density stellar component had to have been in place and to have subsequently been stripped from the dense nuclear star cluster. However, if the low-surface-density spheroidal components are products of star formation in a reionized universe, and the nuclear component is a pre-reionization fossil, then it seems possible that the nuclear cluster-like dense stellar systems could have formed without galaxies surrounding them.

## 7 CONCLUSIONS

We have constructed an analytical model describing star formation in the progenitors of dwarf spheroidal satellite galaxies in the Local Group. The model combines input from published simulations of halo mass assembly in the  $\Lambda$ CDM universe with a star formation prescription consistent with the results of investigations of star formation in gas-rich, low-metallicity dwarf galaxies in the local universe. Our main conclusions are as follows.

Parametrizing the dynamical mass profile of dwarf spheroidal satellite galaxies with  $M_{300}$ , the mass enclosed within the innermost 300 pc, and with the help of the halo concentration dependence on the mass and redshift calibrated by Prada et al. (2012), we derived families of mass-redshift pairs on which the dwarf spheroidals' host halos must have lied at the critical time at which an external tidal field truncated their mass assembly.

Computing the mean most massive progenitor histories for dark-matter-dominated galaxies with the same  $M_{300}$ , thus ostensibly belonging in a common mass scale family, we find that they are similar in the sense that the mean most massive progenitor mass at a fixed redshift  $z$  varies very little among objects with very different masses at the lower redshifts at which their mass assembly was truncated by an external tidal field. This reflects an early assembly of the central 300 pc of the host halos.

The mean most massive progenitor histories of the objects with central densities currently low enough that  $M_{300} \lesssim 10^7 M_\odot$  became able to form stars at lower redshifts than those at which the Local Group is expected to have undergone reionization. Therefore, we conclude that the dwarfs formed most of their stars under reionized conditions. The objects with only somewhat higher central densities  $M_{300} \gtrsim 2 \times 10^7 M_\odot$ , on the other hand, almost certainly formed their first stellar populations before reionization. This led us to hypothesize that it is the temporal relation to reionization that defines the character of a galaxy, whether it will at  $z = 0$  be recognized as a dwarf spheroidal (forming post-reionization), or a different, still to be determined morphological type (forming its first stellar populations before reionization).

Informed by recent numerical investigations of the evolution of halo baryon fractions in a patch of the universe that has experienced reionization, we investigated the dependence of the baryon fraction on the central density parameter  $M_{300}$  and the halo mass and the point at which an external tidal field truncated the mass assembly of these halos. We found that halos with the same  $M_{300}$  have similar baryon fractions independent of the halo mass, but that

the baryon fraction is very sensitive to  $M_{300}$ , dropping by an order of magnitude for a factor of 2 decrease in  $M_{300}$ .

The sensitivity of the baryon fraction to the central density led us to suggest an explanation for why dwarf spheroidal satellites of the Milky Way fall on the approximate common mass scale relation  $M_{300} \approx 10^7 M_\odot$ . The satellite halos with only somewhat lower central densities,  $M_{300} \lesssim 0.5 \times 10^7 M_\odot$ , had baryon fractions too low for a self-shielding HI of a sufficient surface density to have been present in the halo prior to the ram pressure stripping. On the other hand, the satellite halos with only somewhat higher central densities,  $M_{300} \gtrsim 2 \times 10^7 M_\odot$ , commenced efficient star formation before reionization and after the reionization was complete, retained baryon fractions near the cosmic mean. The high baryon fractions meant that the gas in these galaxies was dense enough to form giant molecular clouds, and that it was globally gravitationally unstable. The bar mode instability transported substantial gas masses into the very centers of the latter halos, where it formed stellar systems much more compact than the dwarf spheroidals, but potentially resembling massive globular clusters or the nuclear star clusters in spheroidal galaxies.

Having argued that ionized and warm neutral gas flows in the dwarf spheroidal progenitor objects were both globally and locally gravitationally stable, and that they were partially rotationally supported with disk-like morphologies, we assessed the conditions affecting star formation in these flows (surface densities, metallicities, UV backgrounds) and suggested that the formation of the dwarf spheroidals' stars resembled the star formation currently taking place in the lowest-baryonic-mass dwarf galaxies in the local universe and near the outer edges of late-type disk galaxies. Specifically, the stars formed in the predominantly atomic phase of interstellar medium with a characteristic gas depletion time of  $\sim 10$  Gyr. Metallic fine structure line emission, rather than molecular emission, facilitated the cooling of the gas. We also argued that the star formation proceeded in small units, implying that the resulting feedback should not have had a particularly destructive effect on the gas content of these halos, in contrast with published analyses suggesting intense outflows from dwarf spheroidals' progenitors.

By integrating star formation rates over mean most massive progenitor histories, we computed the stellar masses and half-light radii expected to be found in satellite halos belonging in the common mass scale family  $M_{300} = 10^7 M_\odot$  and representative neighboring families. We found that the stellar mass was a steep, approximately quadratic function of the mass of the progenitor halo at the point of the tidal truncation of mass assembly, just prior to its incorporation into the substructure of the more massive host galaxy. The steepness is a consequence of the strong, approximately linear dependence (at a fixed  $M_{300}$ ) of the time available for star formation on the maximum, tidally truncated mass of the halo.

Allowing for a small  $|\Delta \log M_{300}| \lesssim 0.3$  variation of the central density (and an even smaller variation  $|\Delta \log M_{300}| \lesssim 0.15$  at the low luminosity end), the stellar masses and half-light radii determined from our crude model agree with those observed among the dwarf spheroidals in the Milky Way and Andromeda. The success of the crude model suggests that the ultra-faint dwarfs have exceptionally low stellar masses and high mass-to-light ratios because they formed in relatively low mass, "atomically cooling" halos ( $\sim 10^8 M_\odot$ ) with baryon fractions reduced to  $\sim 10$  per cent of the cosmic mean. The star formation in these objects lasted only  $\lesssim 100$  Myr before the gas was ram pressure stripped.

Pursuing our hypothesis that the chemical enrichment in the dwarf spheroidals' progenitors operated in the lossless regime, we

computed the cumulative enrichment due to the prompt (e.g., core collapse) nucleosynthetic sources. The resulting metallicities exhibit similar magnitudes and a similar scaling with the stellar mass as the observed dwarfs.

## ACKNOWLEDGMENTS

We would like to thank Mia Bovill, Matt McQuinn, and Louis Strigari for useful comments and insightful conversations that have helped us improve the manuscript. We would also like to thank Francesco Prada and Miguel Sánchez-Conde for clarifications on dark matter halo concentrations, Andrei Mesinger, Emanuele Sobacchi, and Takashi Okamoto for clarifications on halo baryon fractions, and Alan McConnachie for advice on interpreting kinematic mass measurements. We also acknowledge helpful conversations with Michael Boylan-Kolchin, James Bullock, Karl Gebhardt, Anatoly Klypin, John Kormendy, Chalence Safrank-Shrader, Risa Wechsler, and Beth Willman. This research was supported by NASA through Astrophysics Theory and Fundamental Physics Program grant NNX09AJ33G and through NSF grant AST-1009928.

## REFERENCES

- Adams, J. J., Uson, J. M., Hill, G. J., & MacQueen, P. J. 2011, *ApJ*, 728, 107
- Agarwal, M., & Milosavljević, M. 2011, *ApJ*, 729, 35
- Ahn, K., Shapiro, P. R., Iliiev, I. T., Mellema, G., & Pen, U.-L. 2009, *ApJ*, 695, 1430
- Arraki, K. S., Klypin, A., More, S., & Trujillo-Gomez, S. 2013, *MNRAS*, 2956
- Babul, A., & Rees, M. J. 1992, *MNRAS*, 255, 346
- Barkana, R., & Loeb, A. 1999, *ApJ*, 523, 54
- Becker, G. D., & Bolton, J. S. 2013, *MNRAS*, 436, 1023
- Begum, A., Chengalur, J. N., Karachentsev, I. D., Kaisin, S. S., & Sharina, M. E. 2006, *MNRAS*, 365, 1220
- Begum, A., Chengalur, J. N., Kennicutt, R. C., Karachentsev, I. D., & Lee, J. C. 2008, *MNRAS*, 383, 809
- Belokurov, V., Zucker, D. B., Evans, N. W., et al. 2006a, *ApJL*, 642, L137
- Belokurov, V., Zucker, D. B., Evans, N. W., et al. 2006b, *ApJL*, 647, L111
- Belokurov, V., Zucker, D. B., Evans, N. W., et al. 2007, *ApJ*, 654, 897
- Benítez-Llambay, A., Navarro, J. F., Abadi, M. G., et al. 2013, *ApJL*, 763, L41
- Benson, A. J., Frenk, C. S., Lacey, C. G., Baugh, C. M., & Cole, S. 2002, *MNRAS*, 333, 177
- Bigiel, F., Leroy, A., Walter, F., et al. 2010, *AJ*, 140, 1194
- Bovill, M. S., & Ricotti, M. 2009, *ApJ*, 693, 1859
- Bovill, M. S., & Ricotti, M. 2011a, *ApJ*, 741, 17
- Bovill, M. S., & Ricotti, M. 2011b, *ApJ*, 741, 18
- Boylan-Kolchin, M., Bullock, J. S., & Kaplinghat, M. 2011, *MNRAS*, 415, L40
- Boylan-Kolchin, M., Bullock, J. S., & Kaplinghat, M. 2012, *MNRAS*, 422, 1203
- Bromm, V., & Yoshida, N. 2011, *ARA&A*, 49, 373
- Brook, C. B., Di Cintio, A., Knebe, A., et al. 2013, [arXiv:1311.5492](https://arxiv.org/abs/1311.5492)
- Brooks, A. M., Kuhlen, M., Zolotov, A., & Hooper, D. 2013, *ApJ*, 765, 22
- Brown, T. M., Tumlinson, J., Geha, M., et al. 2012, *ApJL*, 753, L21
- Bullock, J. S., Kravtsov, A. V., & Weinberg, D. H. 2000, *ApJ*, 539, 517
- Busha, M. T., Alvarez, M. A., Wechsler, R. H., Abel, T., & Strigari, L. E. 2010, *ApJ*, 710, 408
- Cannon, J. M., Giovanelli, R., Haynes, M. P., et al. 2011, *ApJL*, 739, L22
- Christodoulou, D. M., Shlosman, L., & Tohline, J. E. 1995, *ApJ*, 443, 551
- Coleman, M. G., de Jong, J. T. A., Martin, N. F., et al. 2007, *ApJL*, 668, L43
- Cooray, A., & Milosavljević, M. 2005, *ApJL*, 627, L85
- Côté, P., Piatek, S., Ferrarese, L., et al. 2006, *ApJS*, 165, 57
- Crain, R. A., Eke, V. R., Frenk, C. S., et al. 2007, *MNRAS*, 377, 41
- Dalal, N., White, M., Bond, J. R., & Shirokov, A. 2008, *ApJ*, 687, 12
- Dekel, A., Zolotov, A., Tweed, D., et al. 2013, *MNRAS*, 435, 999
- Di Cintio, A., Knebe, A., Libeskind, N. I., et al. 2013, *MNRAS*, 431, 1220
- Dijkstra, M., Haiman, Z., Rees, M. J., & Weinberg, D. H. 2004, *ApJ*, 601, 666
- Dutton, A. A., van den Bosch, F. C., Faber, S. M., et al. 2011, *MNRAS*, 410, 1660
- Fakhouri, O., Ma, C.-P., & Boylan-Kolchin, M. 2010, *MNRAS*, 406, 2267
- Faucher-Giguère, C.-A., Lidz, A., Zaldarriaga, M., & Hernquist, L. 2009, *ApJ*, 703, 1416
- Fialkov, A., Barkana, R., Visbal, E., Tselikhovich, D., & Hirata, C. M. 2013, *MNRAS*, 1307
- Font, A. S., Benson, A. J., Bower, R. G., et al. 2011, *MNRAS*, 417, 1260
- Frebel, A., & Bromm, V. 2012, *ApJ*, 759, 115
- Fridman, A. M., & Poliachenko, V. L. 1984, New York, Springer-Verlag, 1984, 485 p. Translation.
- Gadotti, D. A. 2009, *MNRAS*, 393, 1531
- Gao, L., Theuns, T., Frenk, C. S., et al. 2010, *MNRAS*, 403, 1283
- Garrison-Kimmel, S., Rocha, M., Boylan-Kolchin, M., Bullock, J. S., & Lally, J. 2013, *MNRAS*, 433, 3539
- Geha, M., Brown, T. M., Tumlinson, J., et al. 2013, *ApJ*, 771, 29
- Gilmore, G., Wilkinson, M. I., Wyse, R. F. G., et al. 2007, *ApJ*, 663, 948
- Glover, S. C. O., & Clark, P. C. 2012a, *MNRAS*, 421, 9
- Glover, S. C. O., & Clark, P. C. 2012b, *MNRAS*, 426, 377
- Gnedin, N. Y. 2000, *ApJ*, 542, 535
- Gnedin, N. Y., & Kravtsov, A. V. 2006, *ApJ*, 645, 1054
- Gnedin, N. Y. 2012, *ApJ*, 754, 113
- Governato, F., Zolotov, A., Pontzen, A., et al. 2012, *MNRAS*, 422, 1231
- Grebel, E. K., Gallagher, J. S., III, & Harbeck, D. 2003, *AJ*, 125, 1926
- Grebel, E. K., & Gallagher, J. S., III 2004, *ApJL*, 610, L89
- Greif, T. H., Johnson, J. L., Bromm, V., & Klessen, R. S. 2007, *ApJ*, 670, 1
- Haardt, F., & Madau, P. 2012, *ApJ*, 746, 125
- Hahn, O., Porciani, C., Dekel, A., & Carollo, C. M. 2009, *MNRAS*, 398, 1742
- Holzbauer, L. N., & Furlanetto, S. R. 2012, *MNRAS*, 419, 718
- Hoefl, M., Yepes, G., Gottlöber, S., & Springel, V. 2006, *MNRAS*, 371, 401
- Hopkins, P. F., Cox, T. J., Dutta, S. N., et al. 2009, *ApJS*, 181, 135
- Huang, S., Haynes, M. P., Giovanelli, R., et al. 2012, *AJ*, 143, 133
- Hunter, D. A., Elmegreen, B. G., Oh, S.-H., et al. 2011, *AJ*, 142, 121
- Ianjamasimanana, R., de Blok, W. J. G., Walter, F., & Heald, G. H. 2012, *AJ*, 144, 96
- Ikeuchi, S., Murakami, I., & Rees, M. J. 1989, *PASJ*, 41, 1095
- Irwin, M. J., Belokurov, V., Evans, N. W., et al. 2007, *ApJL*, 656, L13
- Johnson, J. L., Greif, T. H., & Bromm, V. 2008, *MNRAS*, 388, 26
- Kazantzidis, S., Lokas, E. L., Callegari, S., Mayer, L., & Moustakas, L. A. 2011, *ApJ*, 726, 98
- Kepner, J. V., Babul, A., & Spergel, D. N. 1997, *ApJ*, 487, 61
- Kirby, E. N., Lanfranchi, G. A., Simon, J. D., Cohen, J. G., & Guhathakurta, P. 2011a, *ApJ*, 727, 78
- Kirby, E. N., Martin, C. L., & Finlator, K. 2011b, *ApJL*, 742, L25
- Kirby, E. N., Cohen, J. G., Guhathakurta, P., et al. 2013, *ApJ*, 779, 102
- Kirby, E. N., Bullock, J. S., Boylan-Kolchin, M., Kaplinghat, M., & Cohen, J. G. 2014, [arXiv:1401.1208](https://arxiv.org/abs/1401.1208)
- Kitayama, T., & Ikeuchi, S. 2000, *ApJ*, 529, 615
- Kitayama, T., Tajiri, Y., Umemura, M., Susa, H., & Ikeuchi, S. 2000, *MNRAS*, 315, L1
- Kitayama, T., Susa, H., Umemura, M., & Ikeuchi, S. 2001, *MNRAS*, 326, 1353
- Klypin, A. A., Trujillo-Gomez, S., Primack, J. 2011, *ApJ*, 740, 102
- Koposov, S. E., Yoo, J., Rix, H.-W., et al. 2009, *ApJ*, 696, 2179
- Kormendy, J., Fisher, D. B., Cornell, M. E., & Bender, R. 2009, *ApJS*, 182, 216
- Kormendy, J., & Bender, R. 2012, *ApJS*, 198, 2

- Kravtsov, A. V., Gnedin, O. Y., & Klypin, A. A. 2004, *ApJ*, 609, 482
- Kravtsov, A. V., & Gnedin, O. Y. 2005, *ApJ*, 623, 650
- Kravtsov, A. 2010, *Advances in Astronomy*, 2010, 281913
- Kravtsov, A. V. 2013, *ApJL*, 764, L31
- Krumholz, M. R., Leroy, A. K., & McKee, C. F. 2011, *ApJ*, 731, 25
- Krumholz, M. R., & Dekel, A. 2012, *ApJ*, 753, 16
- Krumholz, M. R. 2012, *ApJ*, 759, 9
- Kuhlen, M., Krumholz, M. R., Madau, P., Smith, B. D., & Wise, J. 2012, *ApJ*, 749, 36
- Kuhlen, M., Madau, P., & Krumholz, M. R. 2013, *ApJ*, 776, 34
- Lacey, C., & Cole, S. 1993, *MNRAS*, 262, 627
- Leaman, R. 2012, *AJ*, 144, 183
- Li, T. Y., Alvarez, M. A., Wechsler, R. H., & Abel, T. 2013, arXiv:1306.2971
- Li, Y.-S., De Lucia, G., & Helmi, A. 2010, *MNRAS*, 401, 2036
- Lee, J. C., Kennicutt, R. C., Jr., Funes, S. J. J. G., Sakai, S., & Akiyama, S. 2009, *ApJ*, 692, 1305
- Lewis, A., Challinor, A., & Lasenby, A. 2000, *ApJ*, 538, 473
- Lin, D. N. C., & Faber, S. M. 1983, *ApJL*, 266, L21
- Ludlow, A. D., Navarro, J. F., Li, M., et al. 2012, *MNRAS*, 427, 1322
- Lunnan, R., Vogelsberger, M., Frebel, A., et al. 2012, *ApJ*, 746, 109
- Macciò, A. V., Kang, X., & Moore, B. 2009, *ApJL*, 692, L109
- Macciò, A. V., Kang, X., Fontanot, F., et al. 2010, *MNRAS*, 402, 1995
- Martin, C. L. 1998, *ApJ*, 506, 222
- Martin, C. L. 1999, *ApJ*, 513, 156
- Masaki, S., Fukugita, M., & Yoshida, N. 2012, *ApJ*, 746, 38
- Mayer, L., Governato, F., Colpi, M., et al. 2001a, *ApJL*, 547, L123
- Mayer, L., Governato, F., Colpi, M., et al. 2001b, *ApJ*, 559, 754
- Mayer, L., Mastropietro, C., Wadsley, J., Stadel, J., & Moore, B. 2006, *MNRAS*, 369, 1021
- McConnachie, A. W. 2012, *AJ*, 144, 4
- Mesinger, A., & Dijkstra, M. 2008, *MNRAS*, 390, 1071
- Meylan, G., Sarajedini, A., Jablonka, P., et al. 2001, *AJ*, 122, 830
- Misgeld, I., & Hilker, M. 2011, *MNRAS*, 414, 3699
- Mo, H. J., Mao, S., & White, S. D. M. 1998, *MNRAS*, 295, 319
- Mo, H. J., Yang, X., van den Bosch, F. C., & Katz, N. 2005, *MNRAS*, 363, 1155
- Muñoz, J. A., Madau, P., Loeb, A., & Diemand, J. 2009, *MNRAS*, 400, 1593
- Muñoz, R. R., Geha, M., & Willman, B. 2010, *AJ*, 140, 138
- Navarro, J. F., Frenk, C. S., & White, S. D. M. 1996, *ApJ*, 462, 563
- Neistein, E., van den Bosch, F. C., & Dekel, A. 2006, *MNRAS*, 372, 933
- Noh, Y., & McQuinn, M. 2014, arXiv:1401.0737
- Ocvirk, P., & Aubert, D. 2011, *MNRAS*, 417, L93
- Ocvirk, P., Aubert, D., Chardin, J., et al. 2013, *ApJ*, 777, 51
- Oh, S. P., & Haiman, Z. 2002, *ApJ*, 569, 558
- Okamoto, T., Gao, L., & Theuns, T. 2008, *MNRAS*, 390, 920
- Okamoto, T., & Frenk, C. S. 2009, *MNRAS*, 399, L174
- Okamoto, T., Frenk, C. S., Jenkins, A., & Theuns, T. 2010, *MNRAS*, 406, 208
- Oey, M. S. 2000, *ApJL*, 542, L25
- Oey, M. S. 2003, *MNRAS*, 339, 849
- O'Shea, B. W., & Norman, M. L. 2007, *ApJ*, 654, 66
- O'Shea, B. W., & Norman, M. L. 2008, *ApJ*, 673, 14
- Pan, L., & Scalo, J. 2007, *ApJL*, 654, L29
- Papastergis, E., Martin, A. M., Giovanelli, R., & Haynes, M. P. 2011, *ApJ*, 739, 38
- Pawlik, A. H., Milosavljević, M., & Bromm, V. 2011, *ApJ*, 731, 54
- Pawlik, A. H., Milosavljević, M., & Bromm, V. 2013, *ApJ*, 767, 59
- Planck Collaboration, Ade, P. A. R., Aghanim, N., et al. 2013, arXiv:1303.5076
- Pontzen, A., & Governato, F. 2012, *MNRAS*, 421, 3464
- Prada, F., Klypin, A. A., Cuesta, A. J., Betancort-Rijo, J. E., & Primack, J. 2012, *MNRAS*, 423, 3018
- Purcell, C. W., & Zentner, A. R. 2012, *J. Cosmol. Astropart. Phys.*, 12, 7
- Rashkov, V., Madau, P., Kuhlen, M., & Diemand, J. 2012, *ApJ*, 745, 142
- Read, J. I., Pontzen, A. P., & Viel, M. 2006, *MNRAS*, 371, 885
- Ricotti, M., & Gnedin, N. Y. 2005, *ApJ*, 629, 259
- Ricotti, M. 2009, *MNRAS*, 392, L45
- Ritter, J. S., Safrank-Shrader, C., Gnat, O., Milosavljević, M., & Bromm, V. 2012, *ApJ*, 761, 56
- Roychowdhury, S., Chengalur, J. N., Begum, A., & Karachentsev, I. D. 2010, *MNRAS*, 404, L60
- Roychowdhury, S., Chengalur, J. N., Kaisin, S. S., Begum, A., & Karachentsev, I. D. 2011, *MNRAS*, 414, L55
- Roychowdhury, S., Chengalur, J. N., Karachentsev, I. D., & Kaisina, E. I. 2013, *MNRAS*, 436, L104
- Safrank-Shrader, C., Agarwal, M., Federrath, C., et al. 2012, *MNRAS*, 426, 1159
- Safrank-Shrader, C., Milosavljevic, M., & Bromm, V. 2014, arXiv:1401.0540
- Sakamoto, T., & Hasegawa, T. 2006, *ApJL*, 653, L29
- Salvadori, S., & Ferrara, A. 2009, *MNRAS*, 395, L6
- Saury, E., Miville-Deschênes, M.-A., Hennebelle, P., Audit, E., & Schmidt, W. 2013, arXiv:1301.3446
- Sawala, T., Scannapieco, C., Maio, U., & White, S. 2010, *MNRAS*, 402, 1599
- Schaye, J. 2004, *ApJ*, 609, 667
- Schruba, A., Leroy, A. K., Walter, F., et al. 2011, *AJ*, 142, 37
- Shapiro, P. R., Iliev, I. T., & Raga, A. C. 2004, *MNRAS*, 348, 753
- Simpson, C. M., Bryan, G. L., Johnston, K. V., et al. 2013, *MNRAS*, 428, 1280
- Sobacchi, E., & Mesinger, A. 2013, *MNRAS*, 432, L51
- Sobacchi, E., & Mesinger, A. 2013, *MNRAS*, 432, L51
- Stewart, K. R., Brooks, A. M., Bullock, J. S., et al. 2013, *ApJ*, 769, 74
- Stilp, A. M., Dalcanton, J. J., Warren, S. R., et al. 2013, *ApJ*, 765, 136
- Strigari, L. E., Bullock, J. S., Kaplinghat, M., et al. 2008, *Nature*, 454, 1096
- Strigari, L. E., Frenk, C. S., & White, S. D. M. 2010, *MNRAS*, 408, 2364
- Strigari, L. E., & Wechsler, R. H. 2012, *ApJ*, 749, 75
- Susa, H., & Umemura, M. 2004, *ApJ*, 600, 1
- Swaters, R. A., van Albada, T. S., van der Hulst, J. M., & Sancisi, R. 2002, *A&A*, 390, 829
- Thoul, A. A., & Weinberg, D. H. 1996, *ApJ*, 465, 608
- Tolstoy, E., Hill, V., & Tosi, M. 2009, *ARA&A*, 47, 371
- van Zee, L. 2001, *AJ*, 121, 2003
- Vargas, L. C., Geha, M., Kirby, E. N., & Simon, J. D. 2013, *ApJ*, 767, 134
- Vázquez-Semadeni, E. 2009, arXiv:0902.0820
- Vázquez-Semadeni, E. 2012, *EAS Publications Series*, 56, 39
- Vera-Ciro, C. A., Helmi, A., Starkenburg, E., & Breddels, M. A. 2013, *MNRAS*, 428, 1696
- Walker, M. G., Mateo, M., Olszewski, E. W., et al. 2009, *ApJ*, 704, 1274
- Walsh, S. M., Jerjen, H., & Willman, B. 2007, *ApJL*, 662, L83
- Wang, H. Y., Mo, H. J., & Jing, Y. P. 2007, *MNRAS*, 375, 633
- Wang, J., Frenk, C. S., Navarro, J. F., Gao, L., & Sawala, T. 2012, *MNRAS*, 424, 2715
- Wechsler, R. H., Bullock, J. S., Primack, J. R., Kravtsov, A. V., & Dekel, A. 2002, *ApJ*, 568, 52
- Weisz, D. R., Dolphin, A. E., Dalcanton, J. J., et al. 2011, *ApJ*, 743, 8
- Willman, B., Blanton, M. R., West, A. A., et al. 2005a, *AJ*, 129, 2692
- Willman, B., Dalcanton, J. J., Martinez-Delgado, D., et al. 2005b, *ApJL*, 626, L85
- Willman, B., & Strader, J. 2012, *AJ*, 144, 76
- Wise, J. H., & Abel, T. 2008, *ApJ*, 685, 40
- Wise, J. H., Turk, M. J., Norman, M. L., & Abel, T. 2012, *ApJ*, 745, 50
- Wolcott-Green, J., Haiman, Z., & Bryan, G. L. 2011, *MNRAS*, 418, 838
- Wolf, J., Martinez, G. D., Bullock, J. S., et al. 2010, *MNRAS*, 406, 1220
- Zentner, A. R., & Bullock, J. S. 2003, *ApJ*, 598, 49
- Zhang, H.-X., Hunter, D. A., & Elmegreen, B. G. 2012, *ApJ*, 754, 29
- Zucker, D. B., Belokurov, V., Evans, N. W., et al. 2006, *ApJL*, 643, L103